Master Thesis

Investigation of the Flow Field in an Adaptive Turbine Nozzle with Axial Gap

carried out for the purpose of obtaining the degree of
Master of Science (MSc)
submitted at Technische Universität Wien
Faculty of Mechanical and Industrial Engineering

by

Rouzbeh Karimi, BSc
Mat.Nr.: 1225068

under the supervision of

Ao.Univ.Prof. Dipl.-Ing. Dr.techn. Reinhard Willinger

Institute of Energy Systems and Thermodynamics

February, 2018

Affidavit

I declare in lieu of oath, that I wrote this thesis and performed the associated research myself, using literature cited in this volume. If text passages from sources are used literally, they are marked as such.
I confirm that this work is original and has not been submitted elsewhere for any examination, nor is it currently under consideration for a thesis elsewhere.

Vienna, February, 2018

Signature

Abstract

The present thesis provides an overview of the application, development and problems of rotary valves, which are considered as an alternative concept for controlling of steam mass flow rate in the extraction steam turbines.

The objective of the current work is to perform numerical fluid dynamics investigations on a rotary valve with an axial gap between movable front part and non-movable rear part. In order to determine the effect of this gap on fluid field in the stator of an adaptive turbine stage, Reynolds averaged Navier–Stokes equations (RANS equation) are applied. Furthermore, different turbulence models are compared and subsequently based on the advantages of Shear Stress Transport model (SST) over the other turbulence models such as $k-\epsilon$ and $k-\omega$ models, SST model is selected in the present study. For this purpose, T100 blade profile is chosen and 2D mesh is generated by *ICEM CFD* and flow computation is carried out by *ANSYS CFX*. Thereafter, during the post processing by *ANSYS CFD POST* the flow characteristics, including flow velocity, flow angle, static and total pressure coefficient, loss coefficient and volume flow rate through the gap are investigated, throughout the study for concerning seven different closing degree of rotary valve.

Conclusively, from the computational fluid dynamics (CFD) obtained data are compared with the available experimental data, which were obtained in lab from a rotary valve without gap. Finally a conclusion is drawn in order to indicate the impact of this gap on the flow characteristics.

Kurzfassung

Im Rahmen dieser Diplomarbeit wird ein Überblick gegeben über den Einsatz, die Entwicklung und die Probleme eines Drehschiebers, welcher als alternatives Regelorgan zur Steuerung der Entnahmeparameter bei Entnahmedampfturbinen dient.

Das Ziel dieser Arbeit ist durch eine numerische Strömungsberechnung eines Drehschieberprofils den Einfluss des Axialspaltes auf die Strömung im Leitrad einer adaptiven Turbinenstufe zu bestimmen. Dazu wird das Strömungsgebiet des Profils mittels *ICEM CFD* vernetzt und die ebene Strömung mit *ANSYS CFX* bei sieben verschiedenen Stellungen des Drehschiebers berechnet. Anschließend werden die Strömungscharakteristiken Abströmwinkel, Geschwindigkeitsverhältnis, statischer Druckbeiwert, Totaldruckverlustbeiwert, Verlustbeiwert und Volumenstrom durch den Axialspalt beim Post Processing ermittelt.

Es werden die ermittelten mit den experimentellen Daten, welche durch Untersuchung des Drehschiebers ohne Axialspalt im Labor ermittelt wurden, verglichen und die Auswirkungen des Axialspaltes auf die Strömungscharakteristiken aufgezeigt.

Acknowledgments

The first person whom I would like to gratefully acknowledge is my advisor Ao.Univ.Prof. Dipl.-Ing. Dr.techn. Reinhard Willinger, for his remedial guidance and advices throughout this work. I thank him for his valuable suggestions during this study. He has always been helpful and supportive for me and I found him accommodating and knowledgeable. I would also like to extend my gratitude to my friend, Dipl.-Ing Pejman Hadi Sichani, for his helpful suggestions on this work. Thanks also go to my kind colleague Alexander Lukas Gratzer for his helpful comments.

Last, but certainly not least, I would like to thank my wife M.Sc. Nazak Fakhari for her supports and understanding during my time at work, my parents and my brother for the support they have given me throughout my education.

Contents

1 Introduction **1**

2 Control of Industrial Steam Turbine **2**
2.1 Industrial Extraction Steam Turbines . . . 2
2.2 Control Mechanism . . . 4
2.2.1 Throttle Control . . . 4
2.2.2 Nozzle Group Control . . . 5
2.2.3 Adaptive Control . . . 6
2.3 Rotary Valves . . . 7
2.3.1 Axial Rotary Valves . . . 8
2.3.2 Radial Rotary Valves . . . 10

3 CFD simulation **12**
3.1 Governing Equations . . . 12
3.1.1 Mass Conservation Equation . . . 12
3.1.2 Momentum Conservation Equation . . . 13
3.2 Turbulence Approximation . . . 13
3.2.1 Reynolds Averaged Navier-Stokes Equations . . . 14
3.2.2 Turbulence Models . . . 15
3.3 Geometry Model . . . 19
3.3.1 Blade Profile of Rotary Valve . . . 21
3.3.2 Blade Cascade Geometry . . . 22
3.4 Mesh Generation . . . 25
3.4.1 Wall Treatment . . . 30
3.4.2 Mesh Quality . . . 33
3.5 Boundary Conditions . . . 35
3.5.1 Inlet . . . 36
3.5.2 Outlet . . . 38
3.5.3 Wall . . . 39
3.5.4 Periodic . . . 39
3.6 Fluid Properties . . . 39

4 Results **40**
4.1 Flow Velocity . . . 41
4.2 Flow Angle . . . 44

4.3 Static Pressure Coefficient 52
4.4 Static Pressure Coefficient Distributions on Blade Surfaces 55
4.5 Total Pressure Coefficient 61
4.6 Loss Coefficient 69
4.7 Volume Flow Rate through the Gap 70

5 Conclusion **72**

Bibliography **74**

Nomenclature

Abbreviations

2D	Two Dimensional
3D	Three Dimensional
AS	Adaptive Stage
CFD	Computational Fluid Dynamics
DNS	Direct Numerical Solution
EVM	Eddy Viscosity Model
N-S	Navier-Stokes
RSM	Reynolds Stress Model
RANS	Reynolds Averaged Navier–Stokes
SST	Shear Stress Transport

Greek Symbols

ρ	Density	$[\frac{kg}{m^3}]$
μ	Dynamic Viscosity	[Pa.s]
μ_t	Eddy Viscosity	$[\frac{m^2}{s}]$
η	Efficiency	$[-]$
α	Flow Angle	$[^\circ]$
ζ	Loss Coefficient	$[-]$
$\overline{\alpha}$	Mass Averaged Flow Angle	$[^\circ]$
σ_ϵ	Prandtl Number	$[-]$
ϵ	Rate of Dissipation	$[\frac{m^2}{s^3}]$
τ_{ij}^R	Reynolds Stress Tensor	$[\frac{N}{m^2}]$
λ	Secondary Viscosity Coefficient	$[-]$
ω	Specific Dissipation	$[\frac{1}{s}]$

τ	Shear Stress	$[\frac{N}{m^2}]$

Latin Symbols

b	Axial Chord Length	$[mm]$
f_i	Body Force	[N]
c	Chord Length	$[mm]$
H	Enthalpy Drop (Actual Process)	$[\frac{kg.m^2}{s^2}]$
H_s	Enthalpy Drop (Isentropic Process)	$[\frac{kg.m^2}{s^2}]$
$u_i^{'}$	Fluctuating Velocity	$[\frac{m}{s}]$
u_τ	Friction Velocity	$[\frac{m}{s}]$
g	Gap Width	$[mm]$
$\overline{C}_{pt}$	Mass Averaged Total Pressure Coefficient	$[-]$
y^+	Non-Dimensional Wall Distance	$[-]$
t	Pitch Length	$[mm]$
p_k	Production	$[\frac{m^2}{s^3}]$
p	Static Pressure	[Pa]
C_{ps}	Static Pressure Coefficient	$[-]$
p_t	Total Pressure	[Pa]
C_{pt}	Total Pressure Coefficient	$[-]$
T_k	Turbulent Diffusion	$[\frac{m^2}{s^3}]$
I	Turbulent Intensity	$[-]$
k	Turbulent Kinetic Energy	$[\frac{m^2}{s^2}]$
l	Turbulent Length Scale	$[mm]$
C	Velocity Vector	$[\frac{m}{s}]$
D_k^ν	Viscous Diffusion	$[\frac{m^2}{s^3}]$
Q	Volume Flow Rate through the Gap	$[\frac{m^3}{s}]$
Q_0	Volume Flow Rate through the Inlet	$[\frac{m^3}{s}]$

1 Introduction

Turbomachines are widely used nowadays through the world as power generators, mechanical drives, aircraft and marine engines. Among turbomachines, the steam turbines have been widely employed during the past decades for power generation due to their high efficiencies and low costs. At larger industrial plants the extraction turbines are widely used, which get their name from the fact that steam is extracted at an intermediate point in the turbine casing, at a positive pressure, in order to generate the heat and power to cover the demand of energy in power plant.

In order to use the energy of extracted steam, the reduction of losses and increase the efficiency of turbomachine is necessary. Because the high complexity of loss mechanisms in turbomachines full scale tests are rarely possible, thus the losses must be predicted by using empirical models, which should be determined during the investigation of flow characteristics considering the physical concepts.

Control system of extraction in low pressure part is one of the most important parameters to determine the efficiency of an extraction turbine. Control valves have shown basically reliable operation through control of the extraction parameters. Although they are expensive and need the external actuating. Furthermore high flow loss due to throttling and necessity of maintenance can explain the design of an alternative control element. Rotary valve can be an appropriate alternative control element, which represents improved flow conditions, simple construction, easily function and smaller sizes for installation even lower steam flow losses during mass flow controlling in the turbine [16].

2 Control of Industrial Steam Turbine

This chapter describes the fundamentals of industrial steam turbine control, which are one of the most common prime movers in the world and utilized in a variety of applications in many industries.

2.1 Industrial Extraction Steam Turbines

There are two basic types of steam turbines

1) Condensing turbine

2) Back-pressure turbine.

Figure 2.1 illustrates schematic of these two basic types of steam turbine. Condensing turbines operate with exhaust pressures less than atmospheric pressure, while back-pressure turbines operate with exhaust pressures equal to or greater than atmospheric pressure. Back-pressure turbines get their name from the fact that the pressure of outlet steam depends on the load. As a general rule, condensing turbines tend to be larger in physical size as well as output power. Back-pressure turbines are smaller in physical size than an equivalent condensing unit and usually operate at much higher rotational speeds due to efficiency considerations. A hybrid of the basic condensing and back-pressure turbine is the extraction turbine.

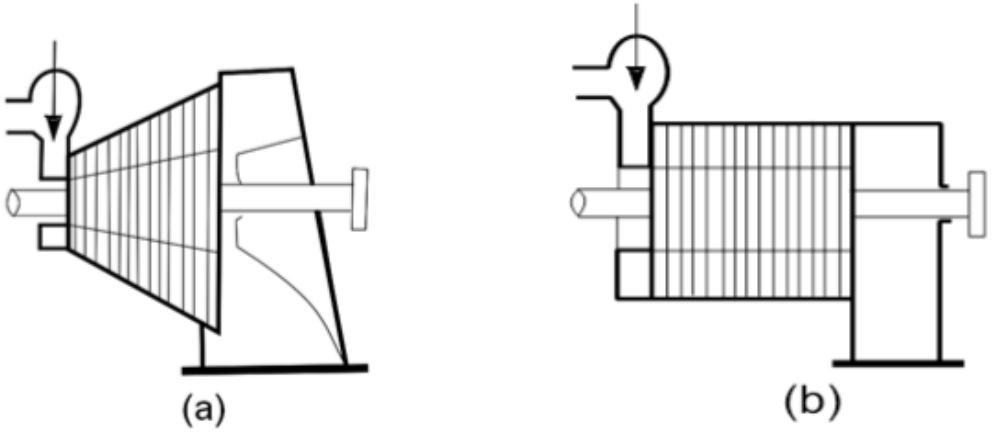

Figure 2.1: Schematic of a) Condensing and b) Back-Pressure Turbines [13]

The extraction condensing turbine contains two outlets as shown in Fig. 2.2. The first outlet extracts the steam with intermediate pressure for the feeding of the heating process while the second outlet extracts the remaining steam with low-pressure steam for the condensation. The extraction of heat from the first outlet can be stopped to generate more output. Steam control valves at this outlet make this steam very flexible and allow adjusting the output as per demand. The steam from the second outlet goes to the condensation chamber, where cooling water brings the temperature of the steam down. Then condensed water goes back to the boiler for the regeneration of the electricity of power. Extraction turbines can be either condensing or back-pressure, depending on the particular application. By extracting steam from the turbine it is avoided to use a pressure reducing valve which is much less efficient. Extraction back-pressure turbines are particularly effective when two or three process steam with different pressure levels are required.

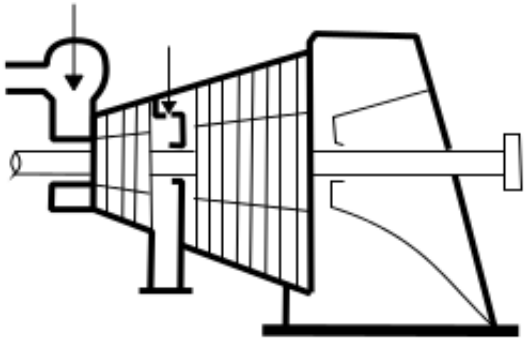

Figure 2.2: Extraction Condensing Turbine [13]

2.2 Control Mechanism

In steam turbine the blades are installed fixed and all of the blade profiles are unmodifiable, therefore reduction of entering steam mass flow rate is the only possibility of control mechanism [10].

2.2.1 Throttle Control

Reduction of total mass flow rate by throttling in the blades cascade is the easiest way of control mechanism in steam turbine (Fig. 2.3).

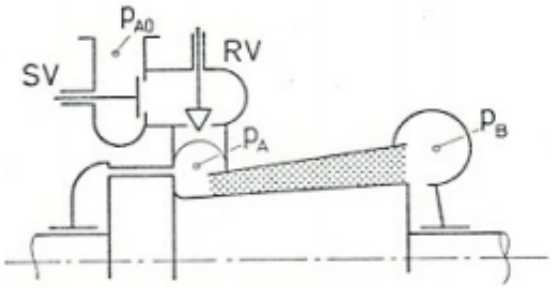

Figure 2.3: Arrangement of Throttle Control. SV Quick-Closing Safety Valve, RV Regulating (Control) Valve [21]

At the entrance of the turbine a quick-closing safety valve is arranged, which gets self-closed by the command of limit-switches. Overspeed and lack of pressure in lubricating oil are the parameters which can activate the quick-closing safety valve.

Pressure p_{A0} is held constant in upstream of the turbine, so that it must be reduced to the p_A after throttling. The disadvantage of throttle control is the internal efficiency reduction (Fig. 2.4). Due to throttle in the control valve, expansion point shifts to the right on the constant pressure line of p_A in $h - s$ diagram ($A_0 \rightarrow A$). Thus heat drop in the turbine is reduced from H_0 to H. The internal efficiency is defined by

$$\eta = \frac{H}{H_s}, \tag{2.1}$$

which decreases with decreasing the value of heat drop. Therefore throttle control in this simple form is used only rarely.

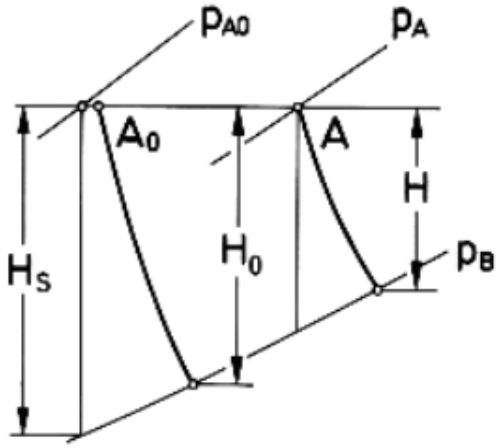

Figure 2.4: Change of the State Characteristics by Throttle Control [21]

2.2.2 Nozzle Group Control

Normally this method is considered to control the mass flow rate in turbine plants which are operating with a constant steam pressure before the turbine. Nozzle group control results in a better part-load efficiency and make a wider range of control in part load operating condition. A disadvantage of this method is low full-load efficiency. Figure 2.5 illustrates the scheme of nozzle group control.

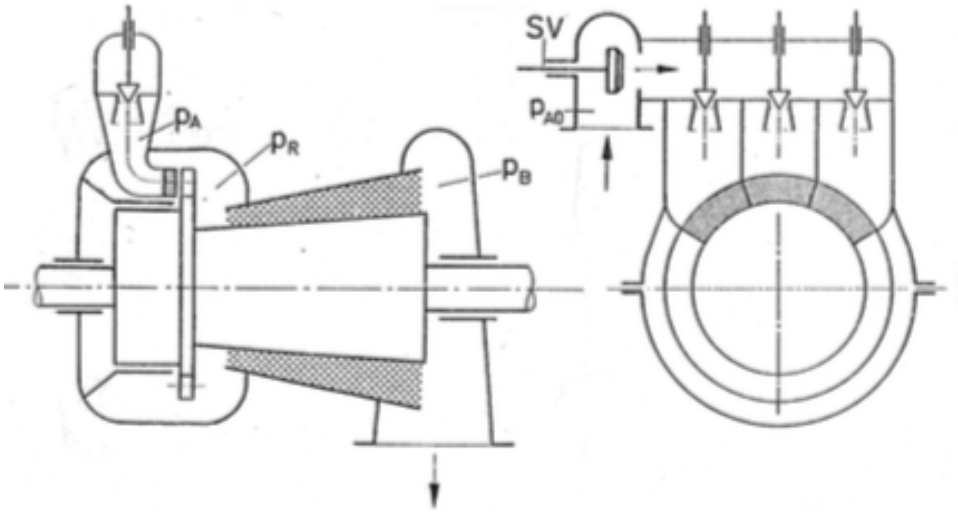

Figure 2.5: Scheme of Nozzle Governing (Three Groups of Nozzles) [21]

2.2.3 Adaptive Control

Adapt the electric energy and heat to variable operating conditions in a cogeneration plant requires application of adaptive control. The main element of adaptive control is the so-called adaptive stage (AS) of flexible geometry located directly downstream of the extraction point (Fig. 2.6).

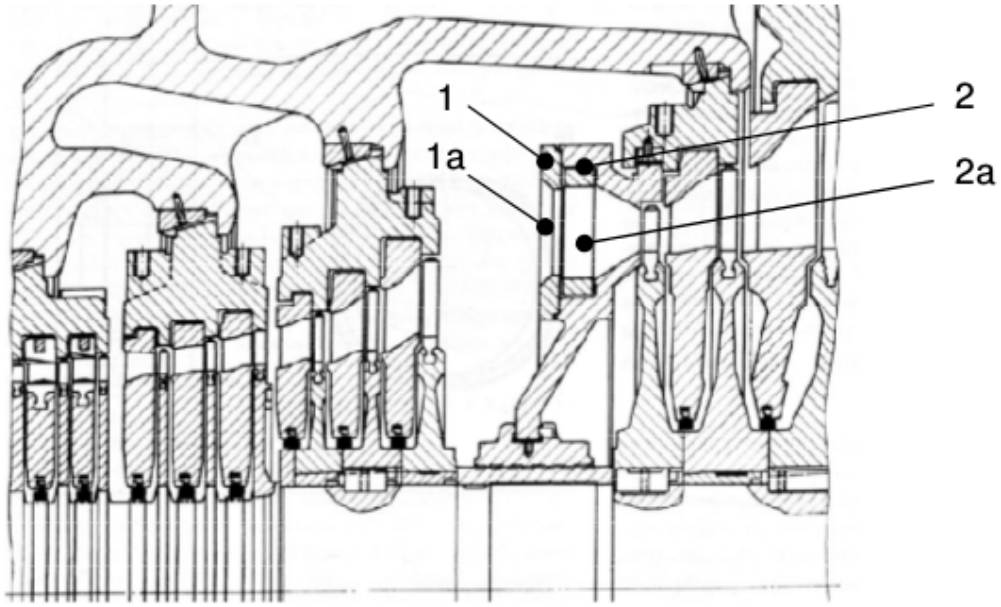

Figure 2.6: Adaptive Stage (AS) Located Downstream of the Extraction Point. Rotating Ring (1), Fix Ring (2) [15]

The most important advantages of adaptive control are usage of the full available pressure drop during the reduction of mass flow rate in the blades cascade and prevent significant increase of enthalpy losses.

Adaptive stage in a steam turbine comprise a fix ring and a slide ring, which are arranged next to each other, whereby the slide ring can rotate relative to the fix ring and block part of the blade-to-blade passage to reduce the mass flow rate (Fig. 2.7).

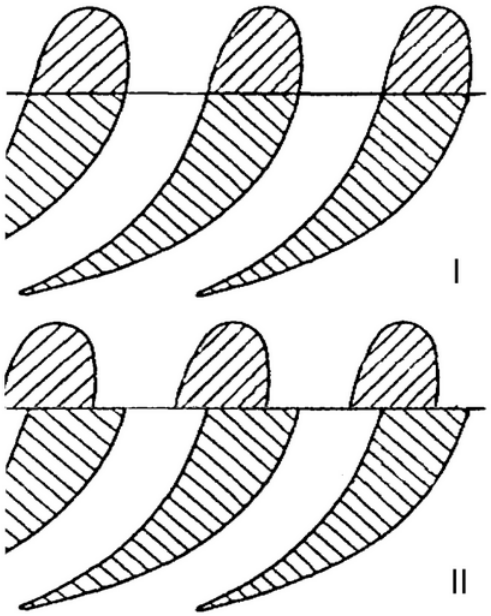

Figure 2.7: Rotary Valve (Nozzles with Movable Front part)
(I) Nozzles Fully Open, (II) Nozzles Partly Open/Closed [10]

2.3 Rotary Valves

Valve is especially a very common used device for throttle control as well as nozzle group control in partial-load because of high reliability, exact operative mechanism and easy installation. However in single casing extraction steam turbine using valve to control the extraction pressure leads to complex structures and mainly inadequate flow conditions, which results in negative effect on the cost, size and efficiency. Therefore, replacement of an adjustable guide blade (Fig. 2.6) is reasonable for control stage, which could be able to regulate the flow through the circumferential passage. Rotary valve is a special type of this alternative construction. There are different types of rotary valves and all of them are exposed to generally same problems and difficulties, particularly high temperature and no possibility of lubrication. In the following section the problems and characteristics of axial an radial rotary valves are described.

2.3.1 Axial Rotary Valves

The rotary valve is arranged so that the coming steam from high-pressure stage of turbine flows directly into the rotary valve. This offers the advantage that the kinetic energy of the steam especially in case of throttle control can be maintained also the low-pressure turbine is always available for energy conversion (Fig. 2.6).

Axial rotary valve can be principally implemented as a throttle control as well as nozzle group control. By throttle controlling are all of the flow cross-sections simultaneously opened or closed. By increasing of profile discontinuities during the closing process, the throttling effect is applied on the total steam mass flow. Due to higher efficiency of rotary valve in the special shape of the flow channel comparing with control valve, throttling effects are preferred (Fig. 2.8). The rotary valve basically consists of a rotating ring (1) and a fix ring (2) with the respective flow channels (1a) and (2a) and a needle roller bearing between rotating ring and fix ring, which causes a gap between them.

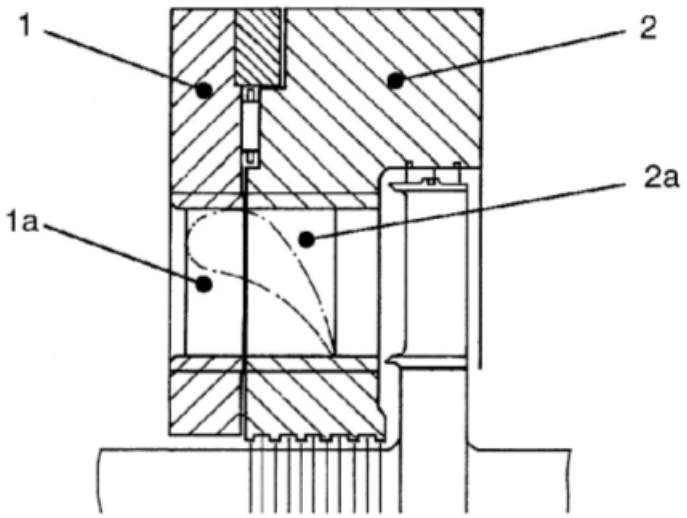

Figure 2.8: Schematic of Axial Rotary Valve for Throttling [5]

Rotating of rotary ring (1) from the fully open position leads to increase of the coverage in flow channel in the fix ring (2a), which results in decreasing of the mass flow.

Using rotary valve in a nozzle group control system (Fig. 2.9), the flow cross-sections are staggered arranged [4]. Here these cut blades are not displaced against each other, but through one slider, the separated nozzle channels are completely or partially opened. The rotary ring (1) is provided with at least two opposite axial control slots (1a). The

underlying channel body (2) has several channel inputs (2a), which are located on the same orbits as the control slots. If the two orbits are in different radial distances, the rotary valve would be closed through a completely 180° rotation.

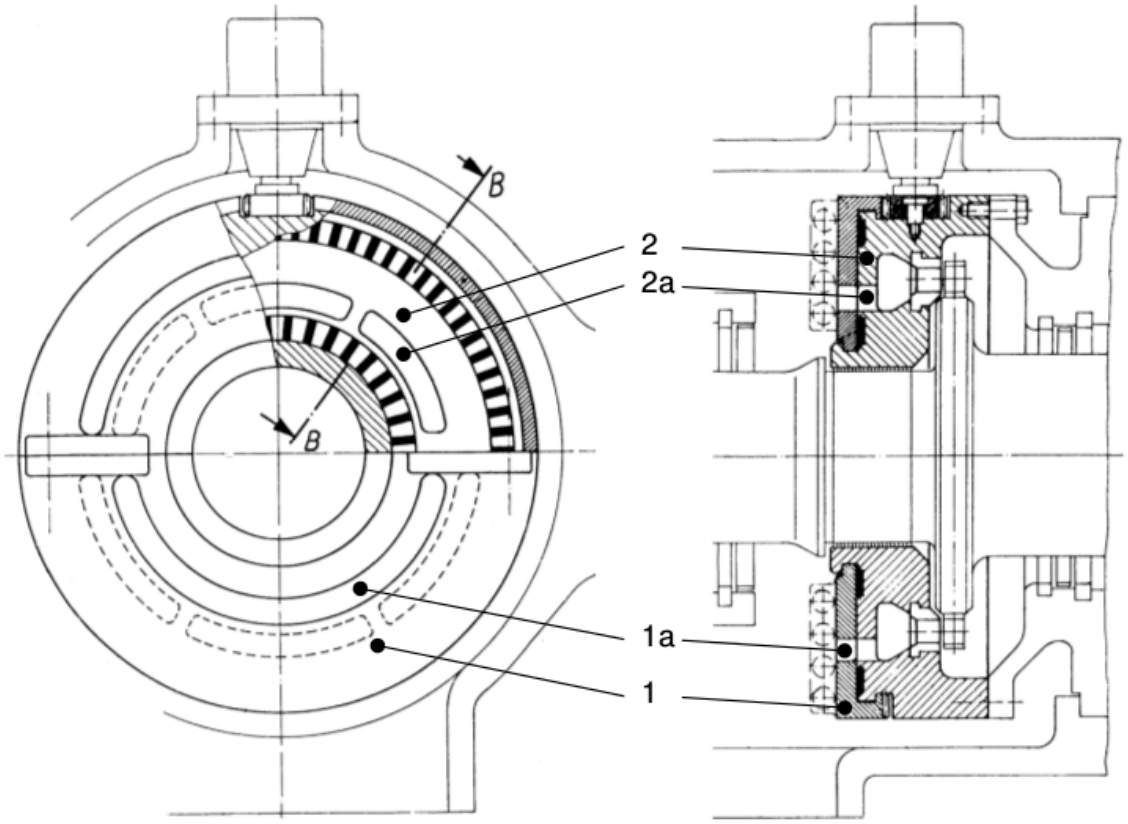

Figure 2.9: Adaptive Stage (AS) Located Downstream of the Extraction Point. Rotating Ring (1), Fix Ring (2) [4]

In partial load condition just the necessary numbers of inputs channels will be fully exposed. For operation states which are between the part-load operating points, each sector is opened only partially by the rotary valve and exposed to a given portion of the mass flow. Therefore, this partial mass flow is only supposed to additional throttling losses which can be kept in a given range. Meanwhile, as the number of exposed sectors, i.e. opened sectors, increase, these additional losses get smaller. In this design type, in order to ensure a better temperature distribution on the casing and the subsequent stator, an opposite opening of the channels is applied. Hereby good partial load efficiencies are achieved like nozzle group control by valve.

2.3.2 Radial Rotary Valves

Similar to axial rotary valve there is an ability in radial rotary valve control to implement as a throttle control as well as nozzle group control. The significant differences between these two types of control is that the fluid medium passes radially and regulated (Fig. 2.10).

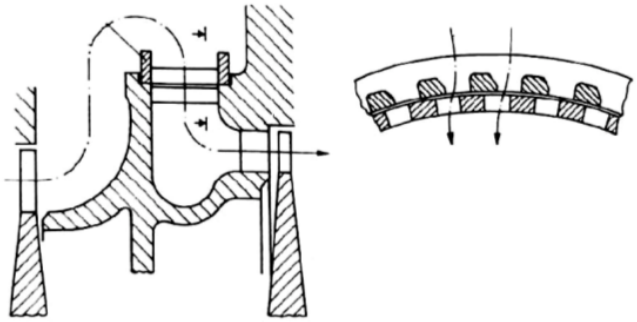

Figure 2.10: Schematic of Radial Rotary Valve for Throttling [16]

Figure 2.11 shows a radial rotary valve for application of nozzle group control. It is apparent that control slots are with an axial offset in the rotating ring (1). The channel body (2), similar to Fig. 2.9, includes again several channel inputs with side by side arrangement (2a) which are opened according to valve position. Both control slots could be applied for completely closing, wherein the control direction is rotated as 180°.

The extraction turbine using radial rotary valve can be seen in Fig. 2.12. It can be seen rotating ring (1), channel body (2) with the respective flow channels (1a) and (2a) and the control equipment which is flanged in the casing.

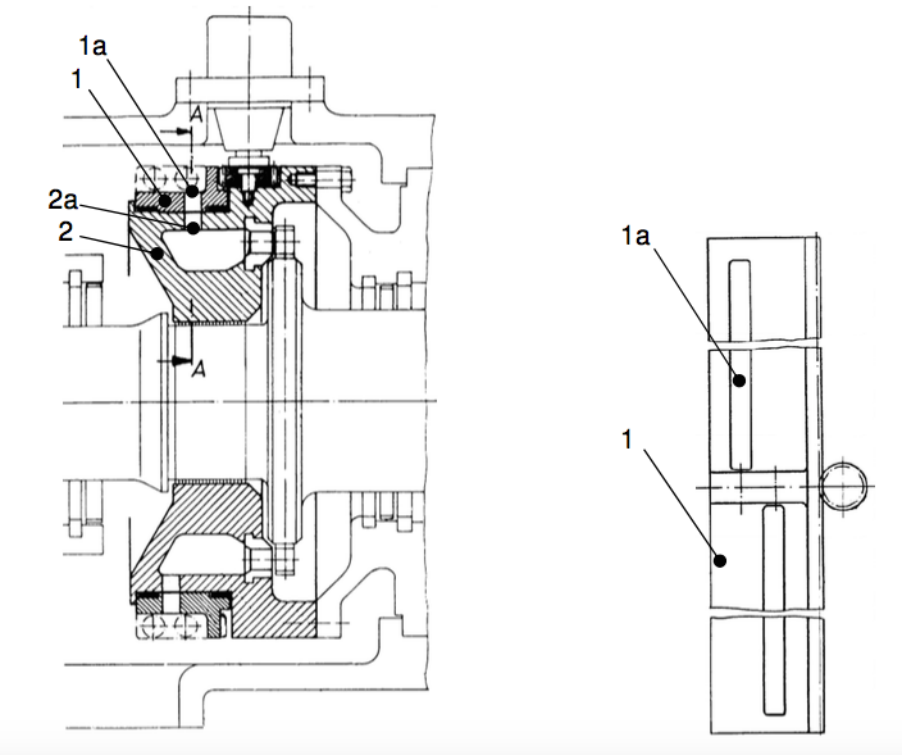

Figure 2.11: Schematic of Radial Rotary Valve for Nozzle Group Control [4]

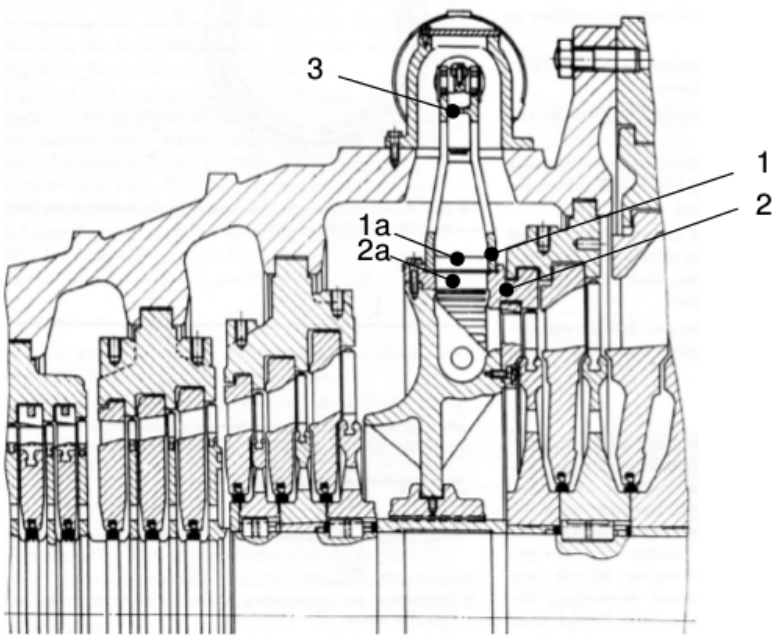

Figure 2.12: Extraction Turbine Using Radial Rotary Valve and its Actuating Mechanism [15]

3 CFD simulation

3.1 Governing Equations

The motion of a fluid can be described by the conservation law for the three basic properties: mass, momentum and energy, which usually is expressed in a set of equations. When the are applied to a perfect viscous fluid, these equations are known as the *Navier-Stokes* equations, while for a perfect inviscid fluid, they are known as *Euler* equations.

In this thesis is assumed that the fluid, which is air at 25°C, is a perfect viscous fluid, furthermore does not happen any heat transfer in domain. Therefore there is not any necessity to solve the energy equation. Hence the mass and momentum conservation equations for incompressible flow in a 2D geometry are considered for the computational domain.

3.1.1 Mass Conservation Equation

The mass conservation equation, also called continuity equation, shows that the variation of mass flow of a fluid system equals to the mass flow passed through the boundary of the system.

$$\frac{\partial \rho}{\partial t} + \frac{\partial \rho u_i}{\partial x_i} = 0, \tag{3.1}$$

where ρ is the mass density, t is time and u_i is the velocity component in x_i .

For incompressible flow, ρ is constant in whole flow field, then Eq. 3.1 can be reduced to the divergence free condition for the velocity [1]

$$\frac{\partial u_i}{\partial x_i} = 0. \tag{3.2}$$

3.1.2 Momentum Conservation Equation

The momentum conservation law is the expression of the generalized *Newton's second law*, defining the equation of motion of a fluid which means that the momentum variation of a fluid system is equal to the total external forces, imposed on it. The momentum conservation equation is given by

$$\frac{\partial u_i}{\partial t} + u_j \frac{\partial u_i}{\partial x_j} = -\frac{1}{\rho}\frac{\partial p}{\partial x_i} + \frac{1}{\rho}\frac{\partial \tau_{ij}}{\partial x_j} + f_i, \tag{3.3}$$

where p denotes the static pressure, τ_{ii} and f_i, $(i = 1, 2)$ are respectively the components of viscous shear stress tensor τ and body force. For $Newtonian\ fluid$, the components of τ are defined by

$$\begin{aligned} \tau_{ii} &= 2\mu\frac{\partial u_i}{\partial x_i} + \lambda\left(\frac{\partial u_i}{\partial x_i} + \frac{\partial u_j}{\partial x_j}\right) \\ \tau_{ij} &= \tau_{ji} = \mu\left(\frac{\partial u_i}{\partial x_j} + \frac{\partial u_j}{\partial x_i}\right),\ i \neq j, \end{aligned} \tag{3.4}$$

where μ is the dynamic viscosity coefficient of fluid and λ is the second viscosity coefficient. The latter is related to a viscous stress caused by the change of the volume, thus it is also called volume viscosity or bulk viscosity. Substituting Eq. 3.4 into Eq. 3.3, considering *Stokes's hypothesis*, the N-S equations of motion is obtained. According to Graves [14], which states that for the majority of fluid flows the shear stress from the volume viscosity can be neglected. For incompressible fluids, the source items can be reduced to the body force f_i. Therefore, N-S equation can be written as [1]

$$\frac{\partial u_i}{\partial t} + u_j \frac{\partial u_i}{\partial x_j} = -\frac{1}{\rho}\frac{\partial p}{\partial x_i} + \nu\frac{\partial^2 u_i}{\partial x_j^2} + f_i. \tag{3.5}$$

3.2 Turbulence Approximation

The approximation of turbulence is a critical numerical method which has been investigated extensively in CFD. Turbulent flow is the most important flow phenomenon in fluid dynamics. It is a flow region characterized by chaotic, stochastic property changes, which includes low momentum diffusion, high momentum convection, rapid variation of pressure and velocity in space and time. Assuming chord length as characteristic dimension, the flow Reynolds number for fully opened position of blades cascade is calculated for 4.15×10^5, which indicates that Reynolds number is higher than critical Reynolds number, hence Flow is turbulent.

Four main numerical methods are developed in order to understand the inner mechanism of turbulence: Reynolds Averaged Navier-Stokes Simulation (RANS), Large Eddy Simulation (LES), Detached Eddy Simulation (DES) and Direct Numerical Simulation (DNS). DNS and LES are excluded for the simulation of complex flow since application of these methods is very expensive and time consuming with current computer technology [6]. Mesh size and time integral scale are much larger in RANS than DNS and LES. As a result, RANS simulations run faster even with smaller computational costs compared to that of DNS and LES. However, some empirical or semi-empirical models, known as turbulence models are required to close the time averaged equations system. Thus the accuracy of RANS simulation to a turbulent flow is heavily limited by the quantity of turbulence model. However, for flows in turbomachinery, RANS is still the dominant simulation method, which in the simulations of this thesis is employed.

3.2.1 Reynolds Averaged Navier-Stokes Equations

Reynolds decomposition is the basic tool to derive the RANS equations from N-S Eq. 3.5.

$$\begin{aligned} u_i &= \overline{u_i} + u_i^{'} \\ p &= \overline{p} + p^{'}. \end{aligned} \tag{3.6}$$

Where $\overline{(...)}$ is a mean (time-averaged) component and $(...)^{'}$ a fluctuating component of a variable. According to Reynolds averaging rules and implementation of Eq. 3.6 in Eq. 3.1 and 3.5, and averaging them in time, results in the Reynolds Averaged mass conservation equation and the RANS equation [7]

$$\begin{aligned} \frac{\partial \overline{u_i}}{\partial x_i} &= 0 \\ \cdot\frac{\partial \overline{u_i}}{\partial t} + \overline{u_j}\frac{\partial \overline{u_i}}{\partial x_j} &= -\frac{1}{\rho}\frac{\partial \overline{p}}{\partial x_i} + \nu\frac{\partial^2 \overline{u_i}}{\partial x_j^2} + \frac{1}{\rho}\frac{\partial \tau_{ij}^R}{\partial x_j}. \end{aligned} \tag{3.7}$$

Where $\tau_{ij}^R = -\rho\overline{u_i^{'}u_j^{'}}$, is called Reynolds stress tensor. It comes from second item on the left hand side (convective item), after Reynolds decomposition and time averaging, due to non-linearity of convective item. It represent the correlation between fluctuating velocities. The expanded format of Reynolds stress tensor is

$$\tau_{ij}^R = -\rho \begin{pmatrix} \overline{u'u'} & \overline{u'v'} & \overline{u'w'} \\ \overline{v'u'} & \overline{v'v'} & \overline{v'w'} \\ \overline{w'u'} & \overline{w'v'} & \overline{w'w'} \end{pmatrix}. \tag{3.8}$$

Reynolds stress tensor introduces 6 additional unknowns in RANS equation. In order to reduce the number of unknowns and equal the number of equations, are further approximations required to represent Reynolds stresses. This can be done by using the turbulence models, which are described briefly in next section.

3.2.2 Turbulence Models

As it is mentioned above, the turbulence models close the Reynolds averaged equations by providing models for the computation of the Reynolds stresses. Turbulence models can be divided into two classes: eddy viscosity models (EVM) and Reynolds stress models (RSM). The eddy viscosity hypothesis assumes that the Reynolds stresses can be related to the mean velocity gradients and eddy (turbulent) viscosity

$$\rho\overline{u_i' \cdot u_j'} = -\mu_t \left(\frac{\partial \overline{u_i}}{\partial x_j} + \frac{\partial \overline{u_j}}{\partial x_i} \right) + \frac{2}{3}\delta_{ij} \left(\rho k + \mu_t \frac{\partial \overline{u_i}}{\partial x_i} \right). \tag{3.9}$$

Where u_i and u_j are the components of mean velocity, μ_t is a scalar property called eddy viscosity and k (Eq. 3.10) is turbulent kinetic energy

$$k = \frac{1}{2} \left(\overline{u_i' u_i'} \right). \tag{3.10}$$

Equation 3.9 is also often called the *Boussinesq hypothesis* or *the Boussinesq approximation*. The advantage of this approach is the relatively low computational cost associated with the computation of the turbulent viscosity (ν_t).

RSM calculate the Reynolds stress tensor directly, using a set of momentum equations of Reynolds stress and an additional scale-determining equation (normally for ϵ). RSM could provide better approximation of turbulence in comparison to EVM. Whereas, the computational efforts of RSM is much larger than that of EVM, which results in a less widely use of RSM compared to EVM in turbomachinary.

According to the number of equations used to determine μ_t, the eddy viscosity models can be classified into zero equation (Algebraic model), One equation model (e.g. Spalart-Allmaras Model) and Two equation models (e.g. $k-\omega$ model and $k-\epsilon$ model). Zero equation models do not have any transport of turbulence, they cannot be expected to accurately predict any flows which have non-local mechanisms. On the other hand zero equation models use the mixing-length model. It requires both empirical deduction of mixing-length (l_{mix}) and the foreknowledge of the $\frac{\partial u_i}{\partial x_j}$, which is recognized as the

weakness of the zero equation model [17].

One equation models use a transport equation of turbulent kinetic energy (k). The transport equation for k is

$$\begin{aligned}
\frac{Dk}{Dt} &= P_k - \epsilon + \Pi_k + T_k + D_k^{\nu} \\
P_k &= -\overline{u_i' u_i'} \frac{\partial u_i}{\partial x_j} \\
\epsilon &= \nu \overline{\left(\frac{\partial u_i'}{\partial x_j}\right)^2} \\
\Pi_k &= -\frac{\partial}{\partial x_i}\left(\overline{\frac{u_i' p'}{\rho}}\right) \\
T_k &= -\frac{\partial}{\partial x_i}\left(\frac{1}{2}\overline{u_j' u_i' u_i'}\right) \\
D_k^{\nu} &= -\frac{\partial}{\partial x_j}\left(\nu \frac{\partial k}{\partial x_j}\right).
\end{aligned} \tag{3.11}$$

Where P_k is the production, ϵ the dissipation, Π_k the pressure diffusion, T_k the turbulent diffusion and D_k^{ν} the viscous diffusion term. One equation models are relatively inaccurate as they describe only k mathematically and they do not improve the predictions greatly compared with the zero equation models, mainly due to the required priori knowledge of the length scale. Moreover, one equation models can not be valid in separated flow regions [11].

Two equation models have less limitation compared to zero equation and one equation models. All of two equation models use the transport equation for k, and they add another transport equation for a second turbulent quantity. The main difference between these models is the choice of this quantity. Generally the second turbulent quantity is of the form [11]

$$\phi = k^m \epsilon^n, \tag{3.12}$$

and the transport equation can be derived by

$$\frac{D\phi}{Dt} = \epsilon^n m k^{m-1} \frac{Dk}{Dt} + \epsilon^{n-1} n k^m \frac{D\epsilon}{Dt}. \tag{3.13}$$

$k-\epsilon$ Model

In this model ϵ (rate of turbulence-energy dissipation) is the second turbulence quantity. Hence $k-\epsilon$ model adds to transport equation of k and ϵ to the governing equations. The exact transport equation of ϵ is given by [2]

$$\frac{D\epsilon}{Dt} = P_\epsilon^1 + P_\epsilon^2 + P_\epsilon^3 + P_\epsilon^4 + T_\epsilon + \Pi_\epsilon + D_\epsilon^\nu - \Phi_\epsilon. \tag{3.14}$$

The terms on right hand side of Eq 3.14 denote the production terms (mixed, mean, gradient and turbulent), diffusion terms (turbulent, pressure and viscous) and Destruction term. The exact form of ϵ transport equation is unacceptably complicated includes large number of not-closed terms. Hence this equation has been modeled and simplified to [8]

$$\frac{D\epsilon}{Dt} = \frac{\partial}{\partial x_j}\left[\left(\nu + \frac{\nu_t}{\sigma_\epsilon}\right)\frac{\partial \epsilon}{\partial x_j}\right] + C_{\epsilon 1}\frac{\epsilon}{k}\nu_\tau\left(\frac{\partial u_i}{\partial x_j} + \frac{\partial u_j}{\partial x_i}\right)\frac{\partial U_i}{\partial x_j} - C_{\epsilon 2}\frac{\epsilon^2}{k}. \tag{3.15}$$

The right hand side of Eq. 3.15 indicates the turbulent diffusion, turbulent production and viscous dissipation.

The modeled transport equation for k is given by [3]

$$\frac{Dk}{Dt} = \frac{\partial}{\partial x_j}\left[\left(\nu + \frac{\nu_t}{\sigma_k}\right)\frac{\partial k}{\partial x_j}\right] + \nu_\tau\left(\frac{\partial U_i}{\partial x_j} + \frac{\partial U_j}{\partial x_i}\right)\frac{\partial U_i}{\partial x_j} - \epsilon, \tag{3.16}$$

where σ_ϵ is Prandtl number, $\sigma_\epsilon = 1.3$, $C_{\epsilon 1} = 1.44$, $C_{\epsilon 2} = 1.92$, $\sigma_k = 1$ and ν_τ is given by

$$\nu_\tau = C_\mu \frac{k^2}{\epsilon}, \tag{3.17}$$

where $C_\mu = 0.09$.

The standard $k-\epsilon$ models are high Reynolds number turbulence models, which permit simulating the turbulence only in the flow core. Furthermore, using this model in adverse pressure gradient and separated flow regions, results in inaccurate results. In order to improve this model some improvements have been made, such as *RNG* $k-\epsilon$ and *realizable* $k-\epsilon$ models, which have been shown higher accuracy compared to *standard* $k-\epsilon$.

$k-\omega$ model

The most popular alternative to ϵ itself is $\phi = \epsilon/k$, The specific dissipation, usually denoted by ω [11], with $m = -1$ and $n = 1$, according to Eq. 3.12. This model shows a better near-wall representation than $k-\epsilon$ model in boundary layer of adverse pressure gradient although $k-\epsilon$ model is more precise than $k-\omega$ in flow core.

Wilcox $k-\omega$ model use another definition for $\omega = \frac{1}{C_\mu}\frac{\epsilon}{k}$. The *Wilcox* $k-\omega$ model consists of the following equations

$$\begin{aligned} \frac{Dk}{Dt} &= P_k + \frac{\partial}{\partial x_j}\left[\left(\nu + \frac{\nu_t}{\sigma_k}\right)\frac{\partial k}{\partial x_j}\right] - C_\mu k\omega \\ \frac{D\omega}{Dt} &= \alpha\frac{\omega}{k}P_k - \beta\omega^2 + \frac{\partial}{\partial x_j}\left[\left(\nu + \frac{\nu_t}{\sigma_\omega}\right)\frac{\partial k}{\partial x_j}\right], \end{aligned} \tag{3.18}$$

where $\nu_t = k/\omega$, $\alpha = 0.55$, $\beta = 0.75$ and $\sigma_k = \sigma_\omega = 2$.

SST Model

Shear Stress Transport (SST) model combines the advantage of both $k-\epsilon$ model and $k-\omega$ model. This turbulence model activates the $k-\omega$ model near the walls and $k-\epsilon$ model for rest of the flow (far from solid surface) using a blending function F_1. If $F_1 = 1$ then $k-\omega$ model is enabled and if $F_1 = 0$ then $k-\epsilon$ model is activated.

The transport equation of k is the same in Eq 3.18 and transport equation of ω consists of the following equation

$$\frac{D\omega}{Dt} = \alpha\frac{\omega}{k}P_k - \beta\omega^2 + \frac{\partial}{\partial x_j}\left[\left(\nu + \frac{\nu_t}{\sigma_\omega}\right)\frac{\partial k}{\partial x_j}\right] + 2\left(1 - F_1\right)\sigma_{\omega 2}\frac{1}{\omega}\frac{\partial k}{\partial x_j}\frac{\partial \omega}{\partial x_j}, \tag{3.19}$$

where $\sigma_{\omega 2} = 1.168$.

SST model uses also an automatic wall treatment, which switches automatically from near-wall treatment to wall function if y^+ is in logarithmic region and vice versa, if y^+ is within the viscous sublayer (Sec. 3.4.1). Therefore it can benefit from near-wall treatment of $k-\omega$ model without the errors resulting from the free stream. Hence in this formulation the accuracy is improved and it is appropriate for a wide range of applications .

As in this work the separated flow is highly expected and due to the mentioned advantages

of SST model in comparison to another models, it is applied as turbulence model in this study.

3.3 Geometry Model

In fully open case (there is not any relative movement between movable front part and non-movable rear part) the numerical analysis of the flow can be carried out either in a domain surrounding a single stator blade profile with periodic boundary lines at midpitch (Fig. 3.1), or in a single flow passage of blade cascade (blade to blade) domain, which uses two blade surfaces, the suction surface of the upper blade and the pressure surface of the lower blade with periodic boundaries leading up to and departing from these surfaces (Fig. 3.5).

In case of closing toward suction or pressure side, due to relatively long pitch length in comparison to distance between the blade surfaces in the cutting position, numerical analysis of the flow in a computational domain surrounding the single blade is impossible. It is for the reason that the periodic boundary line could be located in the vicinity of the blade surface or in cases with high closing degree, the periodic boundary line intersects the edge of blade on the fix part. Figure 3.2 illustrates the computational domain around the blade with 60% closing degree toward pressure side, which is not suitable according to cascade geometry. The above mentioned closing degree is the ratio of shifted moving part to blade thickness, at the cutting position ($x = 0.486\ mm$). In case of closing toward the suction side, the same problem occurs in calculation domain as well. Hence the flow passage of blade cascade is chosen as computational domain for all cases of study.

It should be added, that generally for the common types of steam turbine blades as well as gas turbine blades, which do not have any movement in front part of blade, the other type of computational domain is applied.

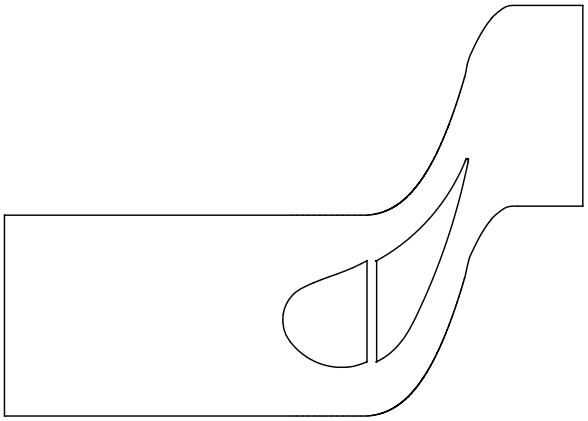

Figure 3.1: Computational Domain around the T100 Blade Profile, Fully Open

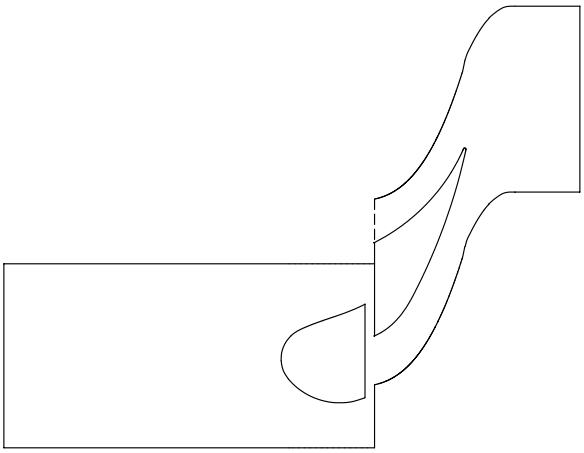

Figure 3.2: Computational Domain Surrounding the T100 Blade Profile, 60% Closing toward Pressure Side

3.3.1 Blade Profile of Rotary Valve

Some aspects must be considered for choosing the blade profile. There are different approaches to choose the as optimal as possible blade profile but often this optimization results in complicated construction of blade. It can be a disadvantage, because the simplicity of the rotating valve will be the great importance. Therefore, in this study T100 blade profile of rotary valve was chosen, considering the simplicity of blade profile [9]. Figure 3.3 illustrates the T100 blade profile of rotary valve with a gap between moving part and fix part. This axial gap is consequence of needle roller bearing, which is located between moving part and fix part of rotary valve, in order to make the rotation of moving part possible. In existing point coordinates of T100 blade profile, axial gap is not considered. In order create the axial gap between moving part and fix part, all point coordinates of fix part are shifted 1 mm to the right side.

The geometrical position of cutting line should be defined through equalization of second moment of inertia (I) between moving part and fix part. Thus the cutting line should be located at 0.486 mm horizontal distance from the blade centroid [9].

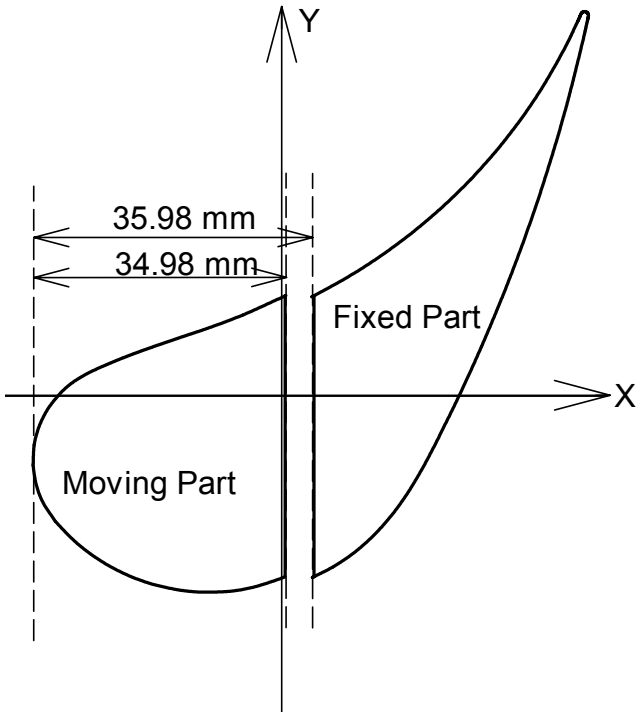

Figure 3.3: T100 Blade Profile, Position of Gap and Cutting Line

As mentioned above, in this work is assumed that the gap width is 1 mm, which is equal to 1% of chord length, 1.25% of pitch length or 3.74% of throat length. although in order

to demonstrate the gap clearly, it is magnified 4 times in Fig. 3.3 and all the others schematic figures.

The cascade nomenclature used in this study is illustrated in Fig. 3.4. Since the pitch length of the purposed geometry should be equal to or less than thickness of blade at the cutting line position, in order to make the complete closing of the flow passage possible. Therefore, T100 blade profile with pitch length of 80 mm is selected. Also this blade has a suitable profile turning shape and proper leading edge radius to fulfill the condition of required blockage for flow.

Parameter	Dimension
Axial chord length, b (mm)	74.05
Chord length, c (mm)	100
Throat length, a (mm)	26.74
Pitch length, t (mm)	80
Gap width, g (mm)	1
Flow Angle, $\alpha\,(^\circ)$	19.53

Table 3.1: Cascade Design Parameters

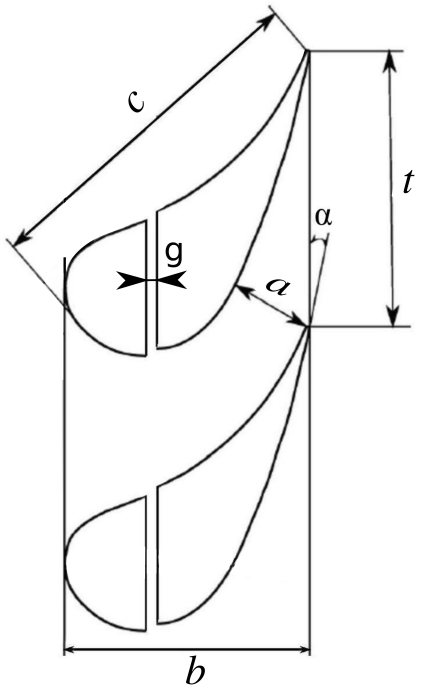

Figure 3.4: Cascade Nomenclature

3.3.2 Blade Cascade Geometry

The coordinate points of T100 blade profile are applied to generate the geometry of blade cascade. There is no gap in the given coordinate points of T100 blade profile. Accordingly, to create the gap between moving part and fix part of blade two points of blade on the pressure side and suction side in exact position of cutting line ($x = 0.486\ mm$) are duplicated and shifted 1 mm to the right side, along with coordinate points of fix part of blade, which contribute to 1 mm gap between moving part and fix part (Fig. 3.5). Afterwards the blade is duplicated and shifted down by applying pitch length ($t = 80\,mm$).

Then the point coordinates of pressure side of upper blade and the point coordinates of suction side of lower blade are deleted. Thus the remaining points demonstrate the point coordinates of a single flow passage in blade cascade.

To create the computational domain, it is necessary to create the inlet and outlet points, which must be distanced from leading edge and trailing edge by at least 1.5 times of chord length ($c = 100\,mm$).

Figures 3.5, 3.6 and 3.7 illustrate respectively the generated computational domain of blade cascade in fully open, closing toward pressure side and closing toward suction side cases with the lines and deleted parts of cascade with dotted lines.

Similarly the point coordinates of moving part of the blade are shifted, for each closing degree, i.e. 20, 40 and 60% of the blade thickness at the cutting position, towards pressure side and suction side. Figures 3.6 and 3.7 illustrate the computational domain for blade cascade in case of closing toward the pressure side and suction side with the lines and deleted parts of cascade with dotted lines.

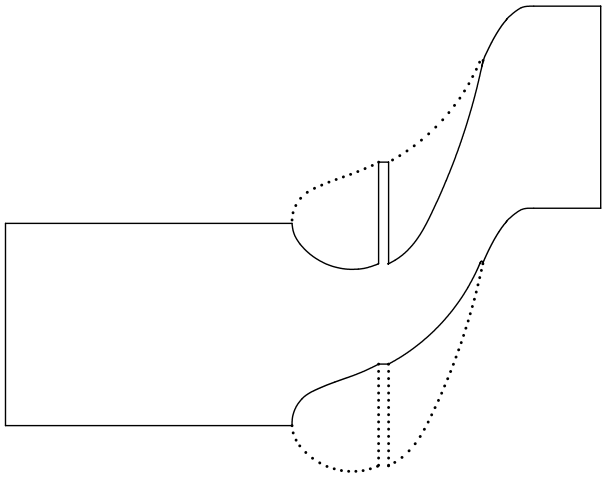

Figure 3.5: Computational Domain for Blades Cascade, Fully Open

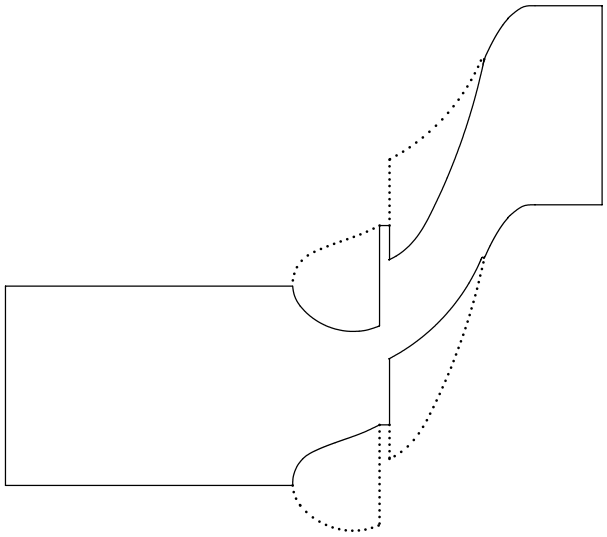

Figure 3.6: Computational Domain for Blades Cascade, Closing toward Pressure Side

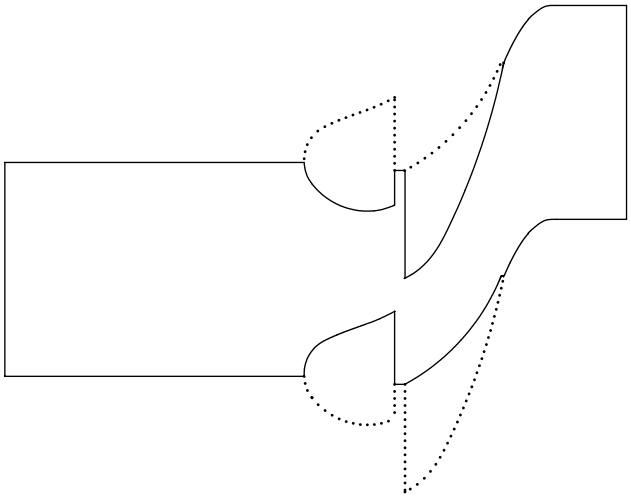

Figure 3.7: Computational Domain for Blades Cascade, Closing toward Suction Side

Afterwards, for all cases, the point coordinates of computational domains are exported in "*.txt*" format and imported to *ANSYS ICEM CFD*. After that the points are connected to each other to create the lines and curves of the computational domain.

3.4 Mesh Generation

In order to solve the N-S equations numerically, the computational domain has to be discretized into a set of non-overlapping volumes (also called cells), which could be polygons, like triangles and quadrilaterals in 2D, and polyhedra, like tetrahedra, pyramids, prisms and hexahedra in 3D. The space discretization forms the so called mesh or grid. The mesh can be built in a structured or an unstructured way. *ANSYS ICEM CFD* can generate the mesh in both ways. Unstructured mesh is more flexible for complicated geometries. Moreover, structured meshes have the capability of fully control of meshing parameters, which is necessary in this model, considering the narrow gap between fix part and moving part which leads to significant difference of geometric scales in computational domain. Accordingly, structured meshes are applied in simulations of this thesis.

For this purpose a primary 2D square-shape block encompasses the whole calculation domain. Then this block is divided into some sub-blocks, in order to adjust the domain. Figure 3.8 illustrates all the sub-blocks that are necessary to generate the mesh. Furthermore, these sub-blocks provide the ability of controlling the mesh in critical regions such as leading edge, trailing edge, near the gap and in the vicinity of blade profile surfaces.

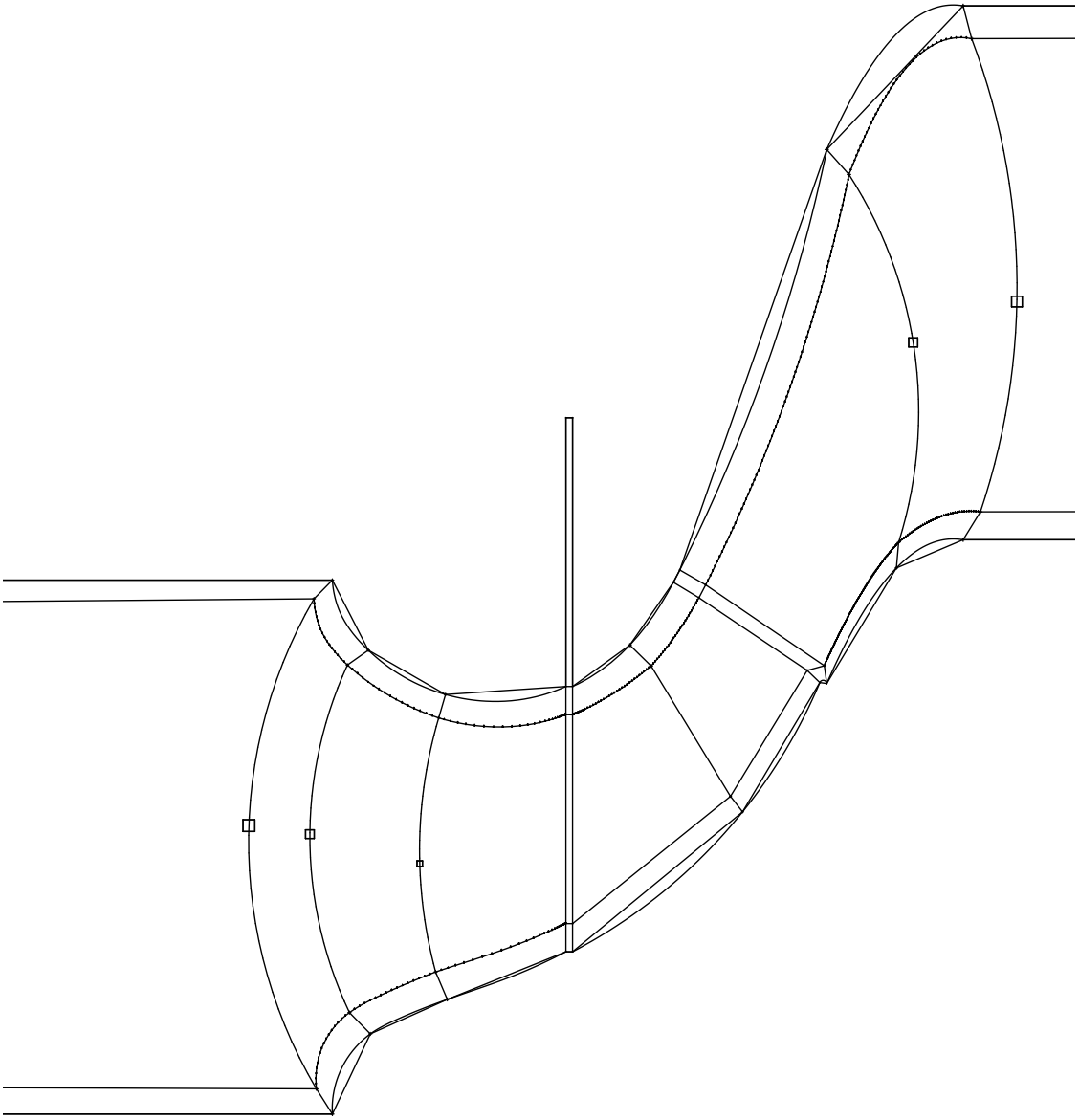

Figure 3.8: Sub-Blocks of Computational Domain, Fully Open

Since the flow velocity gradients are larger in the immediate region close to the walls, the mesh should be significantly finer than the mesh in the region of main stream flow. Thereby, sufficient information is obtained to characterize the gradients in the wall vicinity regions without substantially increasing the total number of mesh nodes in the model which shorten the following calculation time.

Figures 3.9 and 3.10 illustrate meshing of computational domain for fully open and 20% closing toward the suction side case. In Fig. 3.11 the mesh fineness near the walls in

critical areas, such as leading edge where the stagnation occur, trailing edge where wake region arises and the gap between fix part and moving part can be seen.

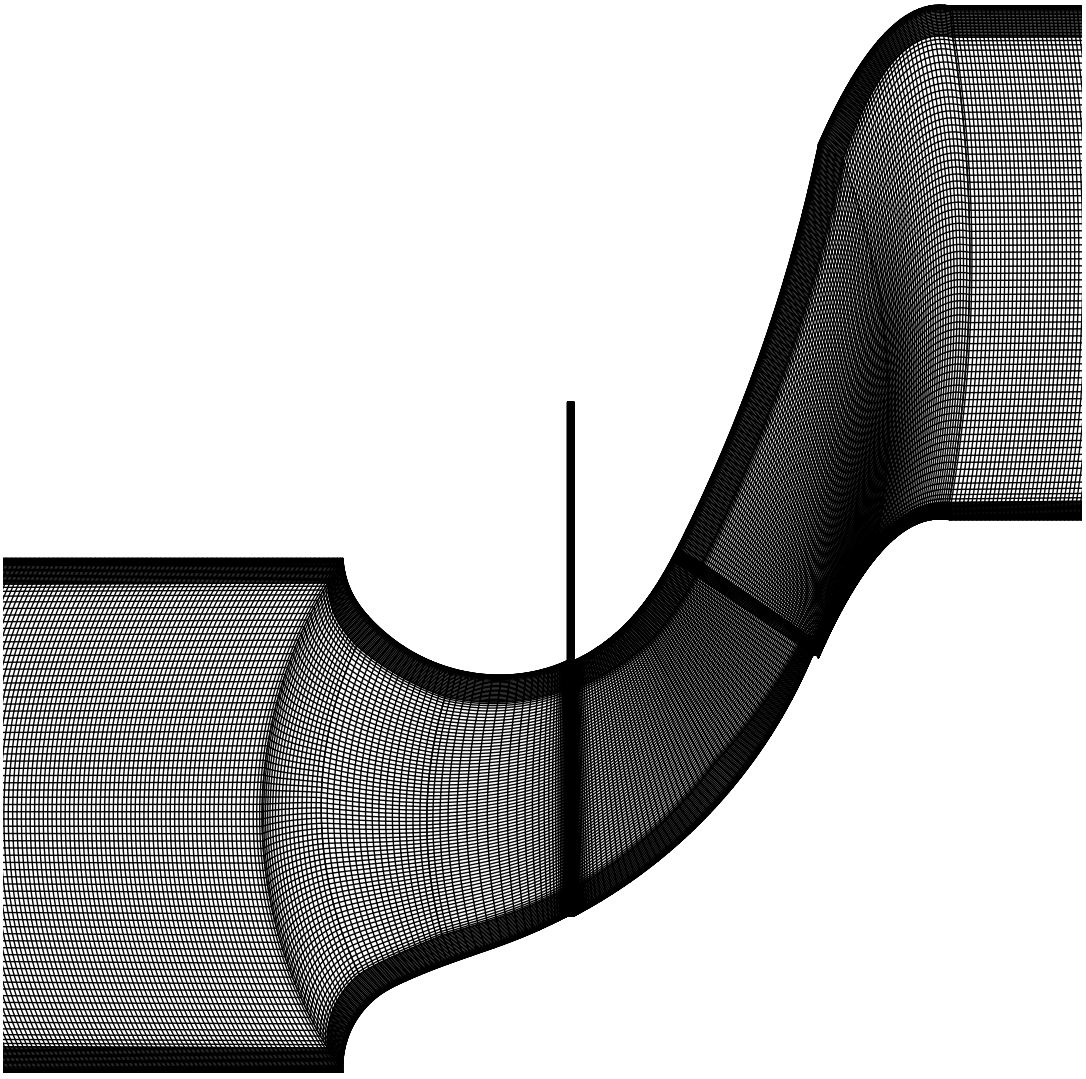

Figure 3.9: Mesh of Blade Cascade, Fully Open

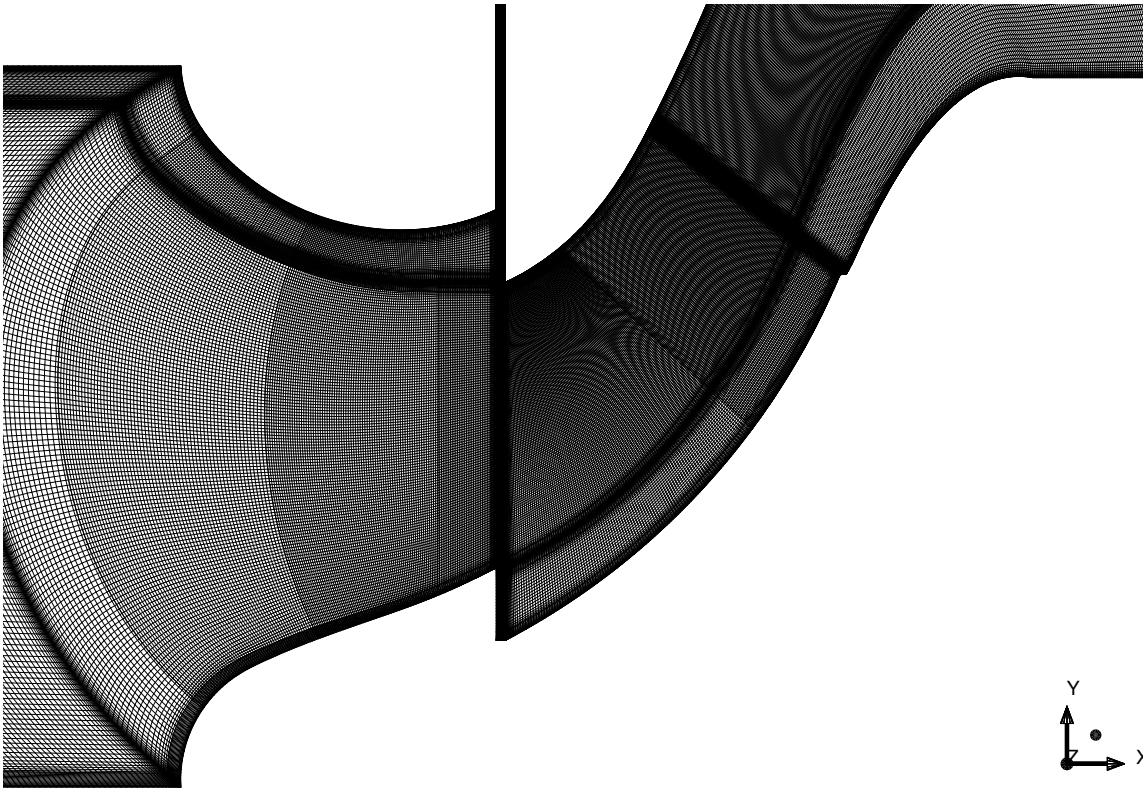

Figure 3.10: Mesh of Blade Cascade, 20% Closing toward Suction Side

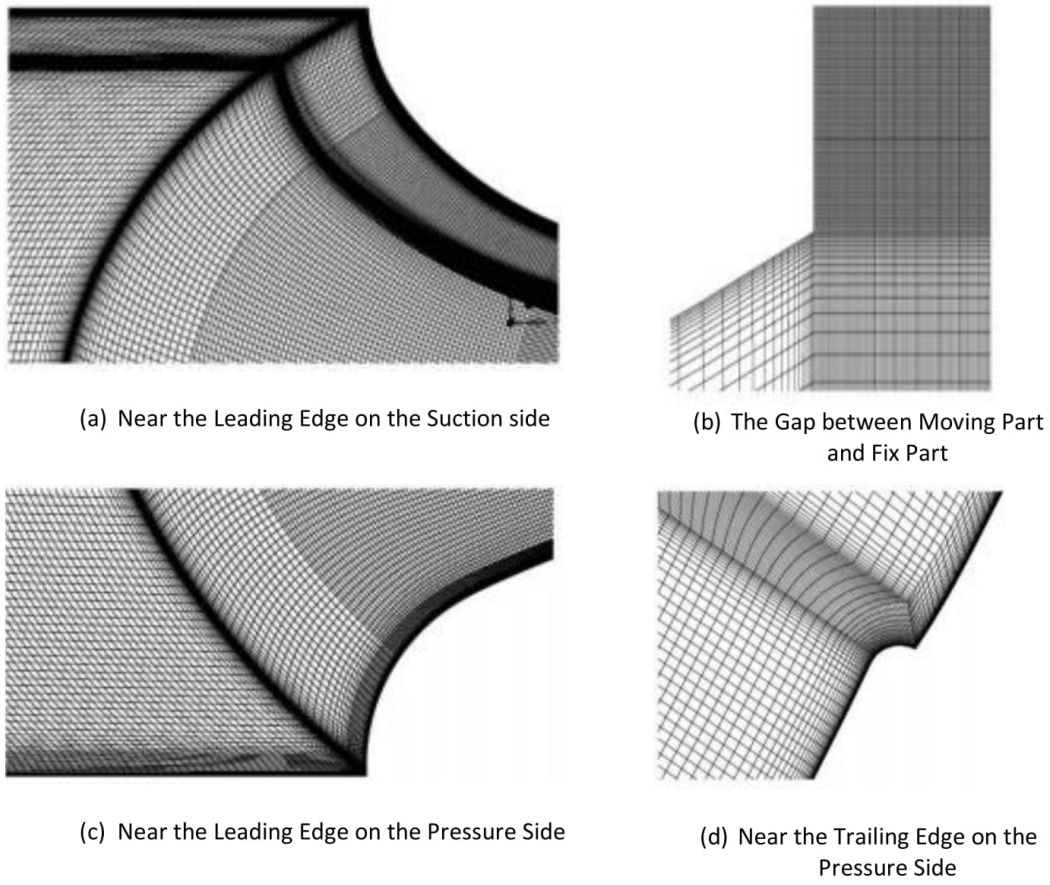

Figure 3.11: Mesh of the Critical Areas in the Computational Domain

As mentioned above the mesh should be fine adjacent to the walls as well as near the leading edge, trailing edge and in the gap which results in the wide range of cell size. Therefore, it is essential to ensure that expansion factor is not greater than 1.2. Expansion factor is the ratio of the surfaces between two neighboring cells. If expansion factor goes over 1.2 it might results in significant errors.

3.4.1 Wall Treatment

As it is mentioned in Sec. 3.2.2, SST turbulence model is applied in this study to compute the Reynolds stress tensor and solve RANS equation. In this model $k - \omega$ model is activated near the wall and $k - \epsilon$ model for the rest of the flow [12]. Turbulence models based on the ω-equation, such as SST model, are suitable for a low-Re method. A low-Re method using fully resolved boundary layers requires a refined boundary layer mesh with very small mesh length scales in the direction normal to the wall. Typically, this requires to ensure that the near-wall node lies at a non-dimensional wall distance smaller than five ($y^+ < 5$) in order to provide an accurate resolution of the flow variables across this layer. $y^+ < 5$ means that the first calculation point will be placed in the viscous sublayer (Fig. 3.12). A non-dimensional wall distance for a wall bounded flow can be defined in the following way

$$y^+ = \frac{u_\tau y}{\nu}, \tag{3.20}$$

where u_τ is the friction velocity, y is the distance to the wall and ν is the local kinematic viscosity of the fluid.

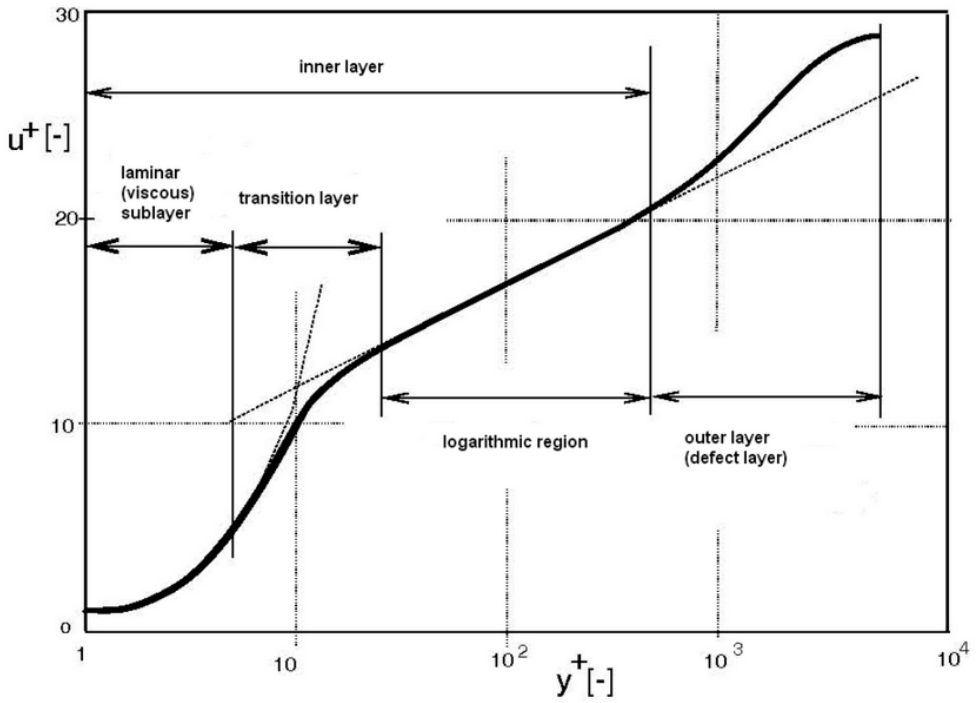

Figure 3.12: Universal Non-Dimensional Velocity Distribution in the Turbulent Boundary Layer [23]

A strict low-Reynolds number model requires a very fine grid resolution. This requirement can hardly be achieved for all walls in complex geometries. It would also lead to excessive cell aspect ratios, which in most cases would require a double precision computation, thereby doubling the memory consumption of the code. If the grid is too coarse, the use of a low-Re model will result in a poor prediction. It is therefore desirable to offer a formulation that switches automatically from wall functions to a low-Re formulation.

The geometry of this study is not too complex, therefore has sought to keep all of the first near-wall cells so fine ($y^+ < 5$) to fulfill the requirement of low-Reynolds number model, since the integration of the boundary layer through the thin viscous sublayer near the wall is preferable to the use of wall function method.

In order to ensure that $y^+ < 5$, an iterative strategy is used. After primary meshing the computational domain and simulating the flow, y^+ must be checked along the walls during post-processing, if y^+ does not lie in the valid range, then the height of the first cell in the direction normal to the wall must be reduced and whole process must be repeated as long as the mesh is fine enough ($y^+ < 5$).

The height of the first near-wall cell is chosen 0.1 mm for the firs step, which resulted to $y^+ > 5$ that means it is a coarse mesh for fully resolution of the boundary layer. The appropriate height of the first near-wall cell for all cases came to 0.01 mm excepting the case of 20% closing toward suction side, which it's appropriate height of the first near-wall cell was 0.005 mm.

Figure 3.13 demonstrates the distribution of y^+ for the first near-wall cell along pressure side and suction side in all cases of closing as well as fully open case. In all cases is along the pressure side and suction side $y^+ < 5$. It can be seen that there is sudden jump in y^+ exactly on the cutting line position of blade. The gap between fix part and moving part leads to discontinuity of geometry on the cutting line position, which leads to higher gradient of velocity in y-direction therefore higher wall shear stress, consequently higher friction velocity which according to Eq. 3.20 leads to higher y^+. It is not necessary to take account of y^+ in this point, which in some cases is over 5 because of discontinuity of geometry. It could be seen that at moving part, y^+ on the pressure side is smaller than this on suction side and vice versa, at fix part, y^+ on the suction side is smaller than this on pressure side. That means generally that viscous sublayer on the suction side of moving part is thinner than this on pressure side, and conversely, in the fix part the viscous sublayer on the suction side is thicker than this on pressure side.

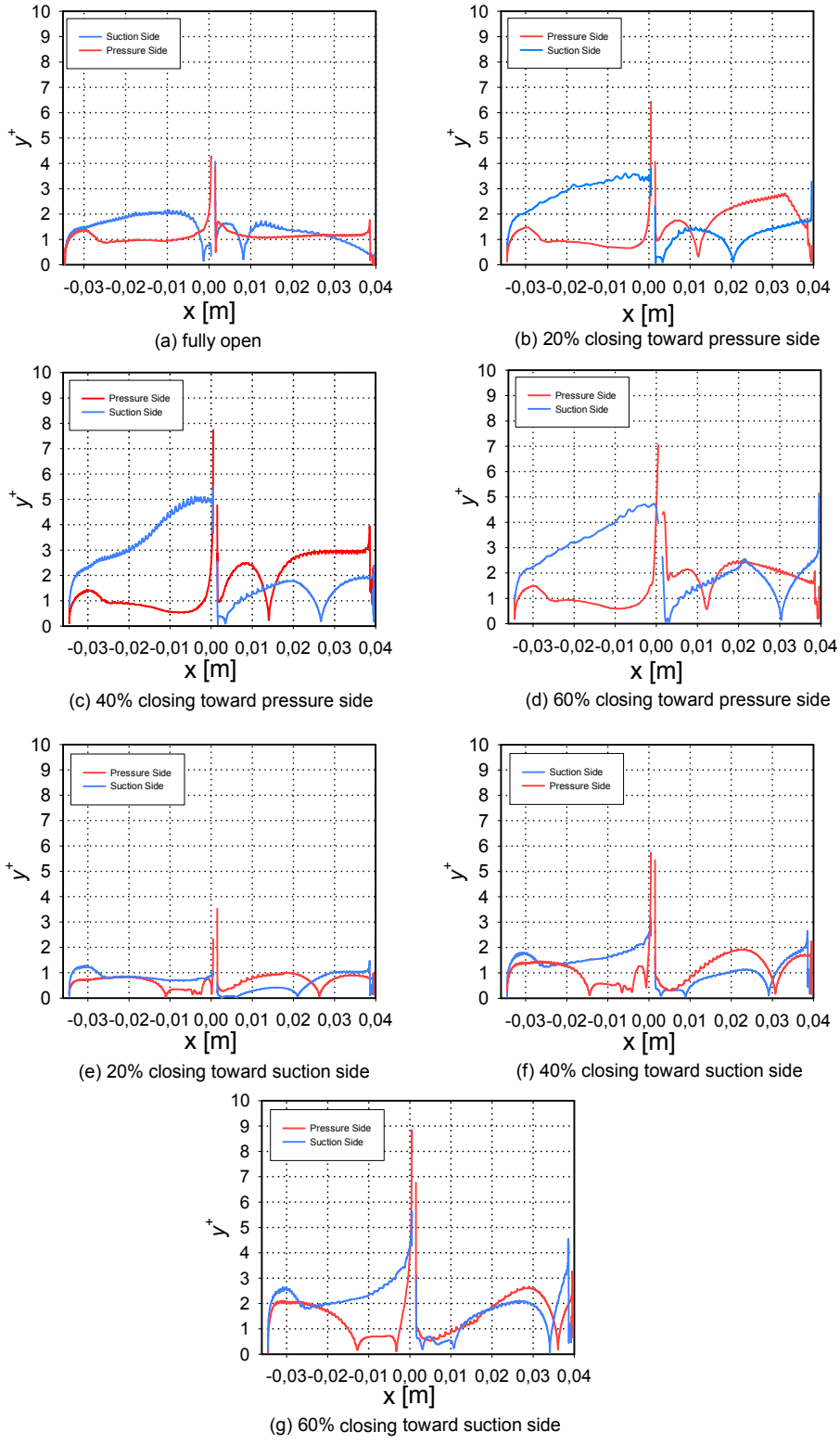

(a) fully open

(b) 20% closing toward pressure side

(c) 40% closing toward pressure side

(d) 60% closing toward pressure side

(e) 20% closing toward suction side

(f) 40% closing toward suction side

(g) 60% closing toward suction side

Figure 3.13: y^+ Distribution on the Pressure Side (Red Line) and on the Suction Side (Blue Line) of Blade Profile

3.4.2 Mesh Quality

Mesh quality issues can have a substantial impact on the solution process in CFD simulation, leading to poor quality solutions, hindering convergence and in some cases, causing the solution to diverge. In order to ensure that generated mesh has high quality, there are some essential mesh quality criterion, such as Aspect ratio, Angle, skewness and Determinant $2 \times 2 \times 2$.

Definition of skewness base on the deviation from a normalized equilateral angle

$$Skewness\ (for\,a\,quad) = max\left[\frac{\theta_{max} - 90}{90}, \frac{90 - \theta_{min}}{90}\right]. \tag{3.21}$$

Where θ_{max} is the largest angle in cell and θ_{min} is the smallest angle in cell. Table 3.2 outlines the overall relationship between skewness and element quality.

Skewness (S)	Quality
S=0	perfect
0.1<S<0.25	excellent
0.25<S<0.5	good
0.5<S<0.75	fair
0.75<S<0.9	poor
0.9<S<1	very poor
S=1	degenerated

Table 3.2: Skewness Mesh Quality

As an average range for all created meshes in this work, more than 95% of the meshes correspond to good and excellent skewness quality ranges and the rest 5% are good or fair, which mostly belong to the region after trailing edge near the lower periodic line (Fig. 3.14).

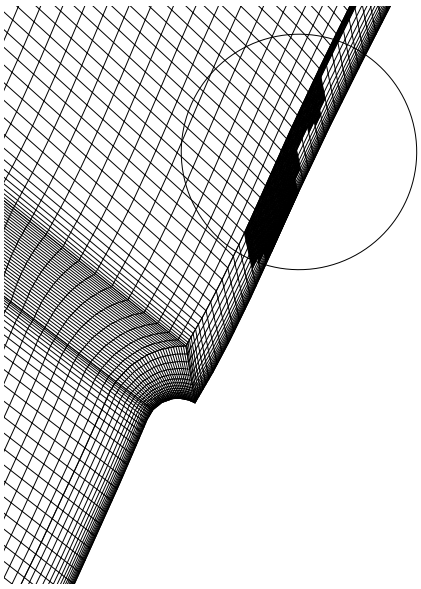

Figure 3.14: Cells with Good Skewness Quality, Located in the Circle, Dyed with Black Color

As it is mentioned above in Sec. 3.4.1 very fine mesh is required near the walls in order to fully resolve the boundary layers but it has to be taken to account that the very fine mesh near the wall in comparison to mesh in main-stream region can result the very high aspect ratio of these cells, which deteriorate the accuracy of solution or causing the solution diverge in extremely high aspect ratios.

Aspect ratio is ratio of longest edge length to shortest edge length (Fig. 3.15).

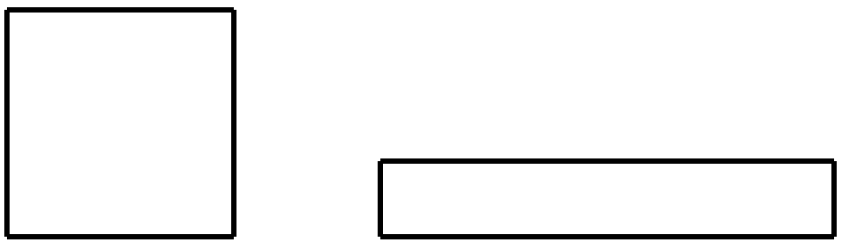

(a) Aspect ratio=1 (b) Aspect ratio>1

Figure 3.15: Aspect Ratio, (a) Ideal for a Square, (b) High Aspect Ratio Quad

The high aspect ratio regions are mostly adjust the walls and consequently they affect the blocks in their upstream and downstream. As an average range for all created meshes in this work, more than 70% of the cells have aspect ratio smaller than 5 and the cells with high aspect ratio do not affect the solution quality, since they are not extremely

high.

The Determinant, more properly defined as the relative determinant, is the ratio of the smallest determinant of the Jacobian matrix divided by the largest determinant of the Jacobian matrix. In this option, the determinant at each corner of the hexahedron is found. The default range is between zero and one. Determinant value of one indicates a perfectly regular mesh element and 0 indicates an element degenerate in one or more edges. Negative values indicate inverted elements [19]. The Determinant value over 0.3 indicates an acceptable quality of mesh element. In this work are Determinant value of all cases over 0.8, which indicates an excellent quality.

The angle quality checks the minimum internal angle for each element. The default range is (0–90) degree, with 0° as degenerate and 90° as perfect quality. The Angle value over 30° indicates an acceptable quality of mesh element. In this work Angle value in all cases for more than 95% of whole cells in computational domain are over 45° which indicates a high angle quality.

Table 3.3 shows the mesh properties for all cases of closing in both directions in detail. It should be mentioned that number of nodes in the gap in x-direction is equal to 101 for all cases of study.

	Number of Nodes in Domain	The Minimum Determinant2×2×2	The Minimum Angle (°)
Fully open	301224	0.934	34.57
20% closing toward pressure side	430632	0.801	27.51
40% closing toward pressure side	467571	0.786	28.01
60% closing toward pressure side	481034	0.835	27.44
20% closing toward suction side	635922	0.930	31.77
40% closing toward suction side	655874	0.933	37.11
60% closing toward suction side	618621	0.924	35.19

Table 3.3: Mesh Properties for All Cases of Study

3.5 Boundary Conditions

In order define a problem that results in a unique solution, information on the dependent (flow) variables at the domain boundaries must be specified. Defining boundary conditions involves identifying the location of the boundaries (e.g. inlet, outlet, wall, symmetry and periodic boundaries) and supplying required information at the boundaries, which depends upon the boundary condition type and the physical models employed.

Figure 3.16 illustrates the location of the boundaries and Tab. 3.4 determine the boundary condition type and the physical models employed according to numbered boundaries in Fig. 3.16.

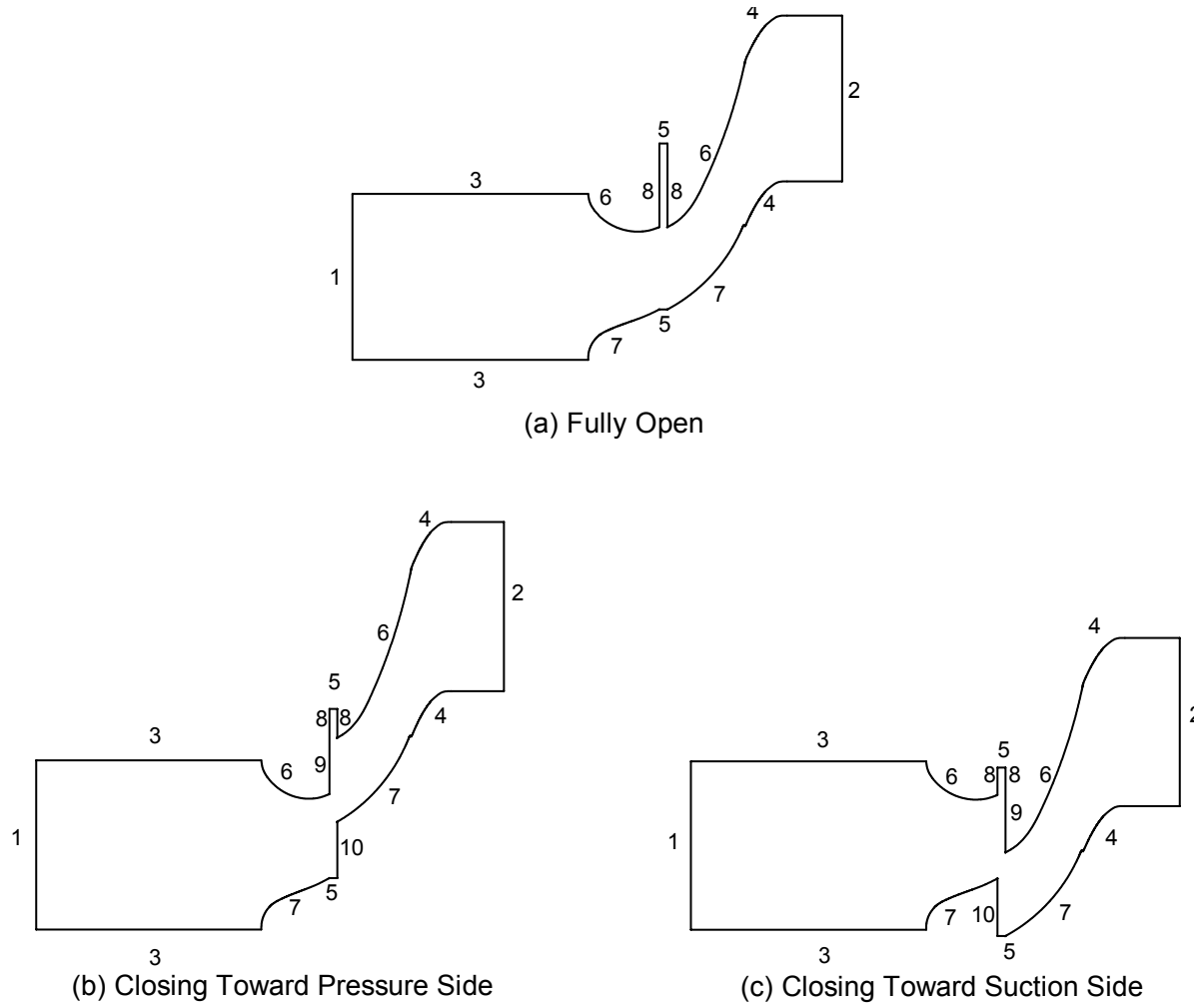

Figure 3.16: Numbered Boundaries of Computational Domain, (a) Fully Open, (b) Closing toward Pressure Side and (c) Closing toward Suction Side

3.5.1 Inlet

The flow variable needs to be specified at the inlet. As it is mentioned that flow is incompressible therefore, velocity inlet is a appropriate type of boundary condition. The velocity inlet boundary condition defines an inflow condition based on the flow velocity.

Numbered Boundary	Boundary Condition
1	Inlet
2	Outlet
3	Inlet periodic
4	Outlet periodic
5	Gap Periodic
6	Wall (suction side)
7	Wall (pressure side)
8	Wall (gap)
9	Wall (edge of suction side)
10	Wall (edge of pressure side)

Table 3.4: Boundary Conditions

In this case, the total (or stagnation) pressure is not fix but will rise (in response to the computed static pressure) to whatever value is necessary to provide the prescribed velocity distribution. In order to make the result of this study comparable to Kariman [9], the same constant value of velocity, normal to inlet boundary (inflow angle is equal to 90°) is set, which is equal to 20 $\frac{m}{s}$.

At the inlet, some quantities are required to specify the transported turbulence according to turbulence model. As it is mentioned above SST $k-\omega$ is applied in this thesis. In order to obtain the turbulent kinetic energy, the following equation can be used

$$k = \frac{3}{2}\left(u_{avg} I\right)^2, \tag{3.22}$$

where u_{avg} is the mean flow velocity and I is the turbulence intensity. Refer to Willinger [22] the turbulence intensity is assumed in all models for 5%.

As is mentioned in Sec. 3.2.2, the Boussinesq hypothesis (Eq. 3.9) is used to relate the Reynolds stresses to the mean velocity gradients [17]. According to Boussinesq approximation, eddy (turbulent) viscosity μ_t is plausibly proportional to k [20]. Furthermore, from dimensional analyses this relation can be written for $k-\omega$ as

$$\mu_t = \frac{\rho k}{\omega}, \tag{3.23}$$

and on the other hand for *Standard* $k-\epsilon$ model this relation can be written as

$$\mu_t = \frac{\rho C_\mu k^2}{\epsilon}. \tag{3.24}$$

Comparing the eddy viscosity in these two equations, the following relation between ω and ϵ can be obtained

$$\omega = \frac{1}{C_\mu}\frac{\epsilon}{k}, \tag{3.25}$$

where C_μ is an empirical constant specified in the turbulence model (approximately 0.09).

The turbulent energy dissipation ϵ, can be defined in terms of turbulent length scale l as

$$\epsilon = C_\mu^{\frac{3}{4}}\frac{k^{\frac{3}{2}}}{l}. \tag{3.26}$$

Comparing Eq. 3.26 and Eq. 3.25, ω can be determined from the following relationship

$$\omega = \frac{1}{C_\mu^{\frac{1}{4}}}\frac{k^{\frac{1}{2}}}{l}. \tag{3.27}$$

This equation is used to determine the turbulence characteristics at the inlet, while the turbulent length scale is assumed for $0.01c$ (l =1 mm).

3.5.2 Outlet

In turbomachinery applications especially in calculation of aerodynamic parameters of the blades cascade is common to select pressure outlet (relative pressure) 0 Pa, for the outlet boundary type. In this manner the average static pressure is activated, which lets the outlet pressure profile vary, while the average value is constrained to the specified value of 0 Pa [18].

3.5.3 Wall

All the blade surfaces are defined as wall. Furthermore no-slip condition is applied to all of them. In this thesis is assumed that all of walls are smooth.

3.5.4 Periodic

These boundary conditions are used to simulate processes in a small part of a large system with repeated pattern. For this condition, it is then mandatory to select two boundary faces that will be treated as if they are physically connected. The flow exits/enters one periodic boundary then enters/exits the other periodic boundary. Periodic functionality plays a key role in properly analyzing rotating machinery applications. As it is mentioned above, a linear cascade is utilized in this thesis, therefore a translational periodicity is applied.

3.6 Fluid Properties

The fluid domain used for this simulation contains air at $25°C$, which is specified as an incompressible fluid. Fluid properties for air at $25°C$ with constant specific heat capacities are given in Tab. 3.5.

property	**Value**
Temperature $[°C]$	25
Density $[\frac{kg}{m^3}]$	1.185
Specific Heat Capacity $[\frac{J}{Kgk}]$	1004.4
Dynamic Viscosity $[\frac{Kg}{ms}]$	1.831×10^{-5}
Molar Mass $[\frac{Kg}{kmol}]$	28.966

Table 3.5: Fluid Properties of the Air

According to Kariman [9] the Mach number of outflow is calculated less than 0.3. Thus the flow is subsonic and the assumption of incompressible flow is taken for all simulations.

4 Results

The simulations results are presented and discussed in the current chapter. The main interest of this chapter is the impact of the gap on the 2D passage flow in different cases of closing toward suction side and pressure side, i.e. fully open, 20%, 40% and 60% are investigated. For this reason, the dimensionless form of flow characteristics, such as flow velocity, flow angle, static pressure coefficient C_{ps}, total pressure coefficient C_{pt} and loss coefficient are considered meticulously. Additionally the volume flow rate of air through the gap is studied in all cases. In order to evaluate the outflow characteristics, a line is generated in downstream of flow, at 6 mm distance from the trailing edge (Fig. 4.1).

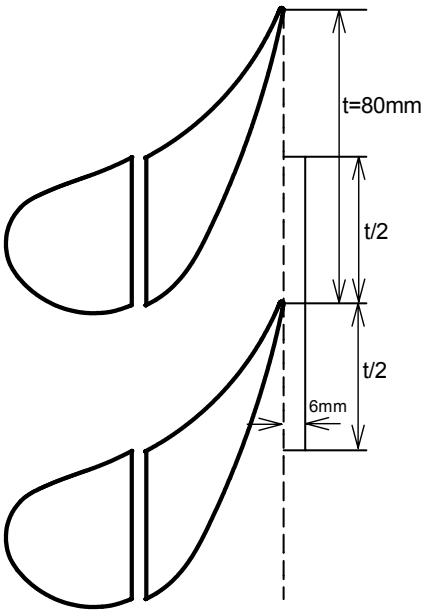

Figure 4.1: Position of Measurement line, 6 mm Downstream of Trailing Edge

As mentioned in Sec. 3.3 it is not possible to generate the computational domain around a blade. Therefore, the computational domain is generated in flow passage. However there is not such difficulties in lab. Hence the measurement line in lab is located 6 mm downstream of a single blade. In order to make the simulation results comparable to

experiment results, they are shifted $t/2$ (40 mm) downwards. Figure 4.1 illustrates the shifted measurement line 6 mm downstream of trailing edge. In order to make the plots more comprehensible, all variables are made dimensionless. Hence the measurement line is divided by pitch length ($t = 80\ mm$) to make the x-axis dimensionless. Besides the x-components of blade profile are divided by axial chord length ($b = 74.05\ mm$).

4.1 Flow Velocity

In order to make the flow velocity dimensionless, velocity magnitude is divided by inlet velocity C_0 which is defined as boundary condition at the inlet ($C_0 = 20\ m/s$). Hence the comparison of normalized velocity with different boundary conditions would be easier, specially for different inflow velocity.

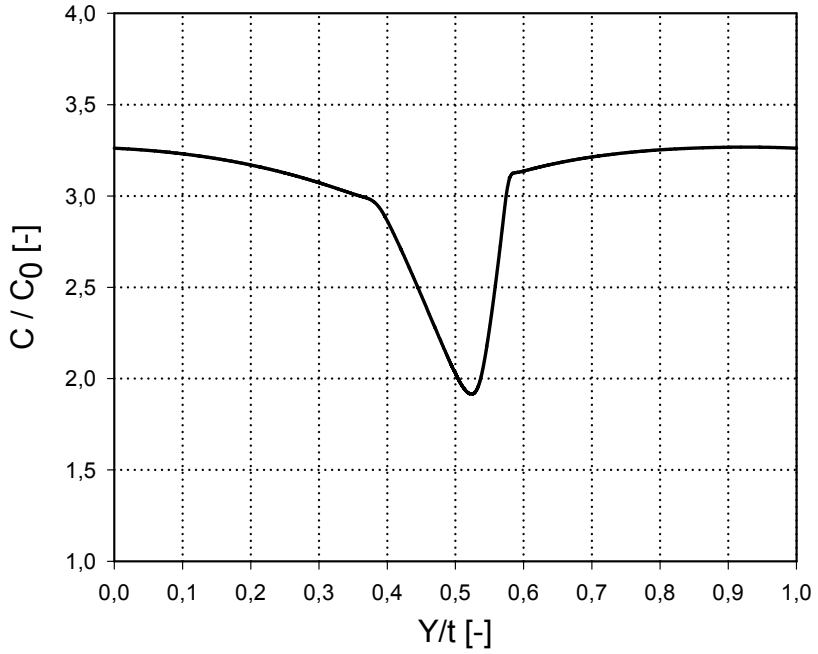

Figure 4.2: Pitchwise Flow Velocity, Fully Open, 6 mm Downstream of Trailing Edge

Figure 4.2 illustrates the pitchwise distribution of flow velocity in case of fully open. It can be seen that the pitchwise velocity is almost constant within the inviscid flow region, i.e. the flow outside the boundary layers. The reason of the normalized velocity fall is the develop of boundary layer from blade surfaces to downstream of blade profile which occurs around $0.4 < Y/t < 0.6$. This region is called wake region or viscous wake. The fluid could not be assumed frictionless any more in wake region. Here can be seen that the wake region in fully open case is not perfectly symmetric and is shifted slightly to the

right. This means that the thickness of boundary layer on suction side develops quicker than that on pressure side or, the separation on suction side affects the wake region. Comparing the CFD results of flow velocity in this thesis with Kariman [9] shows a slight difference for a fully open case, which is marginally smaller than the one without axial gap between moving part and fix part. It is considerable that the wake region in cascade without gap shows more symmetric distribution of velocity, which could be the impact of gap. So the presence of gap can result in non-uniformed development of boundary layers on suction side and pressure side.

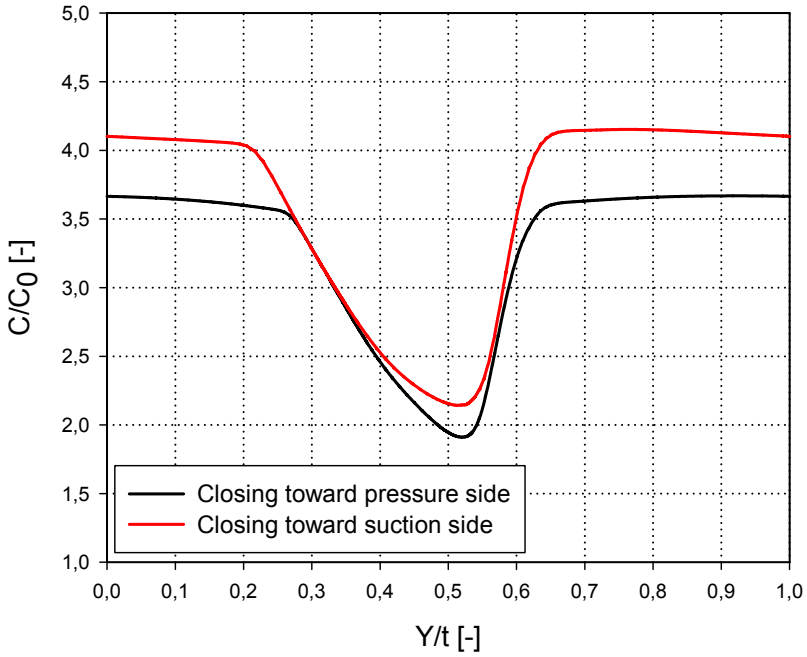

Figure 4.3: Pitchwise Flow Velocity, 20% Closing toward Pressure Side and Suction Side, 6 mm Downstream of Trailing Edge

Figure 4.3 compares the distribution of flow velocity for 20% closing toward pressure side and suction side. The range of velocity for closing toward suction side is higher than the one for closing toward pressure side. Furthermore, it can be seen that the flow velocity is greater than that for fully open case, since the flow is incompressible and with decrease of cross section area during closing process the velocity should increase. It is clearly visible, that the pitchwise width of wake region for 20% closing is wider than that for fully open case. It means that closing process results in thicker boundary layer and separation region. In both closing directions, the wake region is not perfectly symmetry.

Figures 4.4 and 4.5 compare higher closing degrees, i.e. 40% and 60%. These figures demonstrate that higher closing degrees can contribute to higher flow velocity and also result in wider pitchwise wake region.

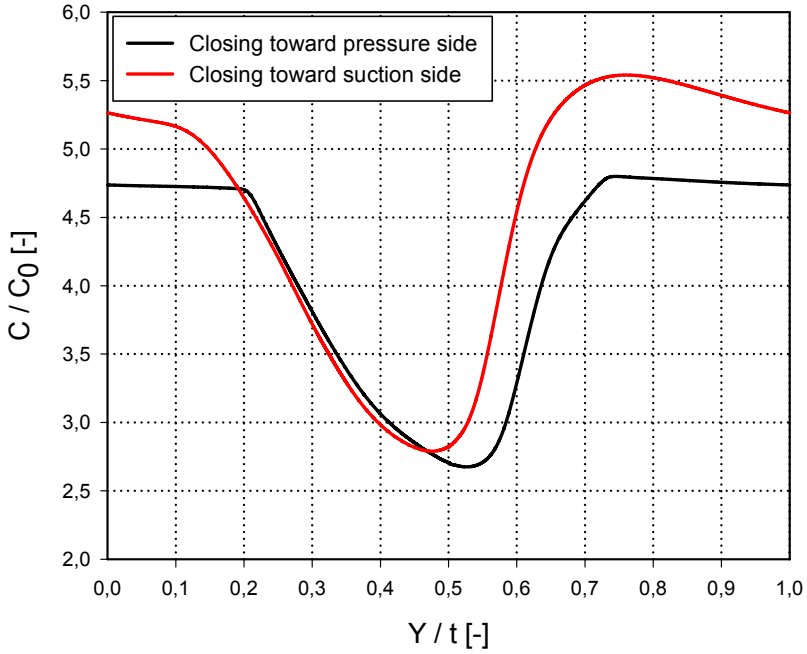

Figure 4.4: Pitchwise Flow Velocity, 40% Closing toward Pressure Side and Suction Side, 6 *mm* Downstream of Trailing Edge

It is important to note that the distribution of velocity for 60% closing toward pressure side does not show the noted 'V' shape distribution of velocity, but more sinus shape. This could be the consequence of pressure side boundary layer and suction side boundary layer merging. This act causes elimination of inviscid flow region, which means the whole pitchwise measurement line is affected by friction.

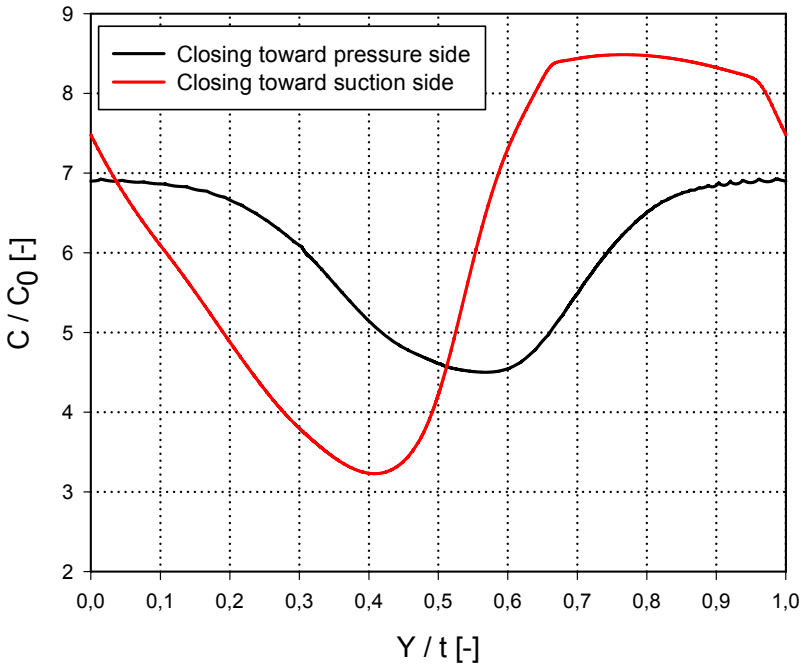

Figure 4.5: Pitchwise Flow Velocity, 60% Closing toward Pressure Side and Suction Side, 6 mm Downstream of Trailing Edge

4.2 Flow Angle

In this section flow angle for different cases of study, i.e. fully open and closing toward suction side and pressure side, is investigated. The flow angle is calculated from

$$\alpha = \arctan\left(\frac{C_x}{C_y}\right), \tag{4.1}$$

where C_x is the x-component and C_y is th y-component of velocity vector.

Figure 4.6 illustrates the pitchwise flow angle in a fully open case. It is conspicuous that the maximum angle appears near the trailing edge, which is around 23°. The wedge angle of blade causes this increase. It can be seen that in inviscid region, i.e. $Y/t < 0.4$ and $Y/t > 0.6$ the flow angle decreases and in wake region, i.e. $0.4 < Y/t < 0.6$ tends to increase.
It should be mentioned that the measurement line is relatively close to trailing edge, that can have an impact on flow angle because of separated flow specially on the suction side.

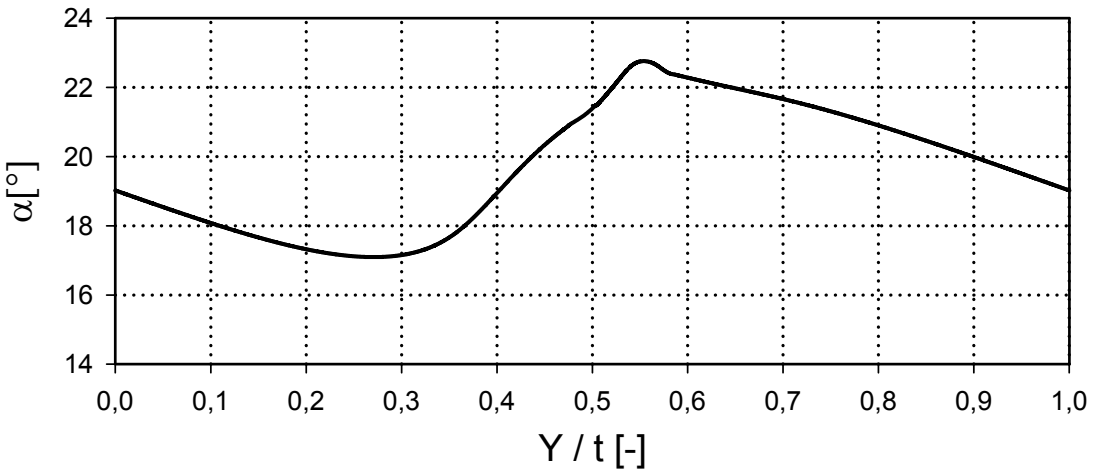

Figure 4.6: Pitchwise Flow Angle, Fully Open, 6 *mm* Downstream of Trailing Edge

The comparison between Fig. 4.6 with [9] signifies that in both cases the maximum of flow angle is near the trailing edge but in the present case of study (with a gap between fix part and moving part) this maximum value is greater than the one without gap. The reason could be as follows: the flow of the gap after entering to the flow passage causes a separation and affects the boundary layer on the suction side (Fig. 4.7). Such a flow can influence the flow angle in downstream of the cascade.

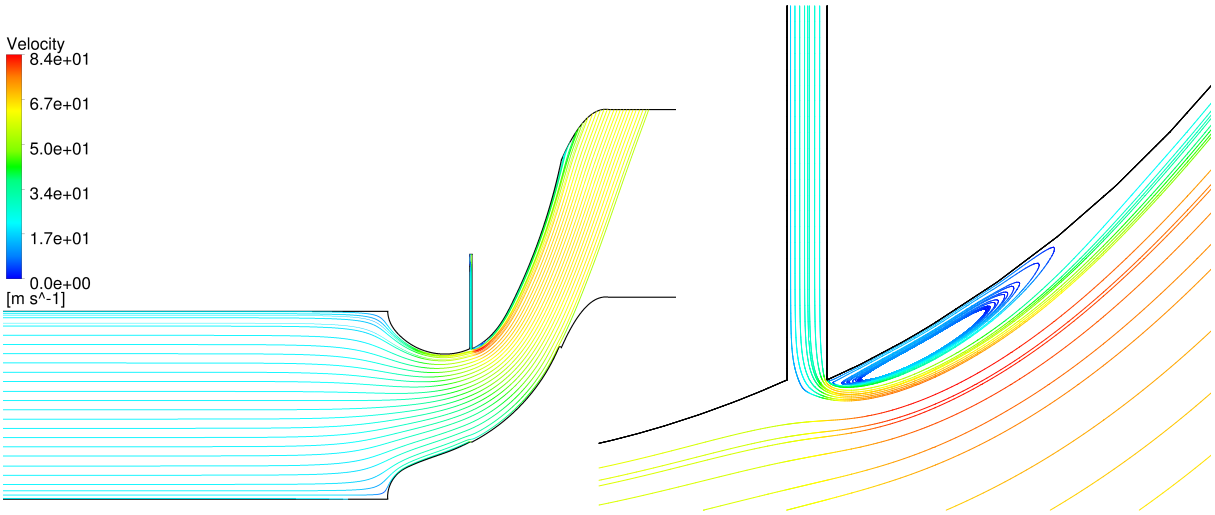

Figure 4.7: Streamline Patterns in the Flow Passage, Fully Open

Figure 4.8 illustrates that the overall trend of flow angle for 20% closing in both directions, are similar to fully open case, although the fully open case shows greater flow angle, particularly compared to closing toward suction side.

It can be seen in Fig. 4.9 that the flow angle for closing toward pressure side deviates slightly along measurement line. In terms of closing toward suction side, it can be seen that the flow angle in wake region is not constant but in inviscid flow region, i.e. $Y/t < 0.2$ and $Y/t > 0.8$ is approximately constant.

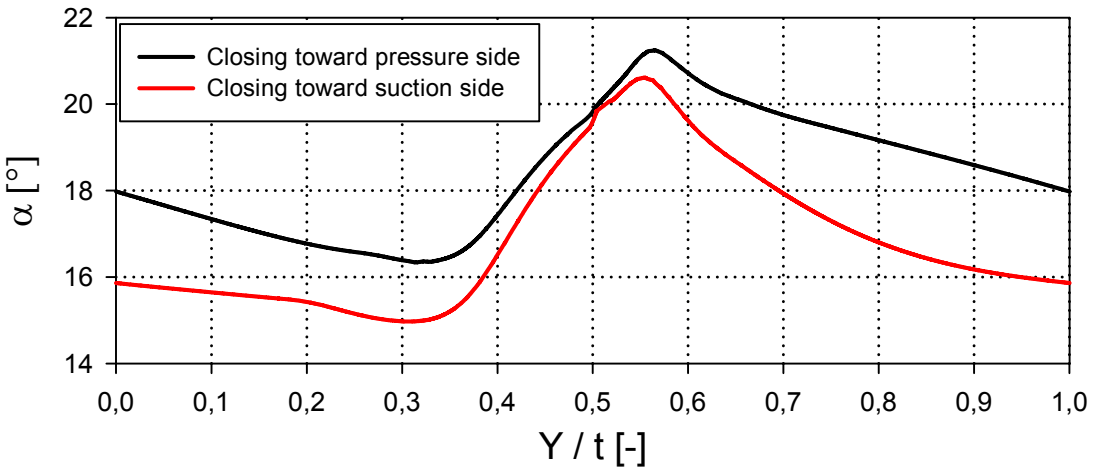

Figure 4.8: Pitchwise Flow Angle, 20% Closing toward Pressure Side and Suction Side, 6 *mm* Downstream of Trailing Edge

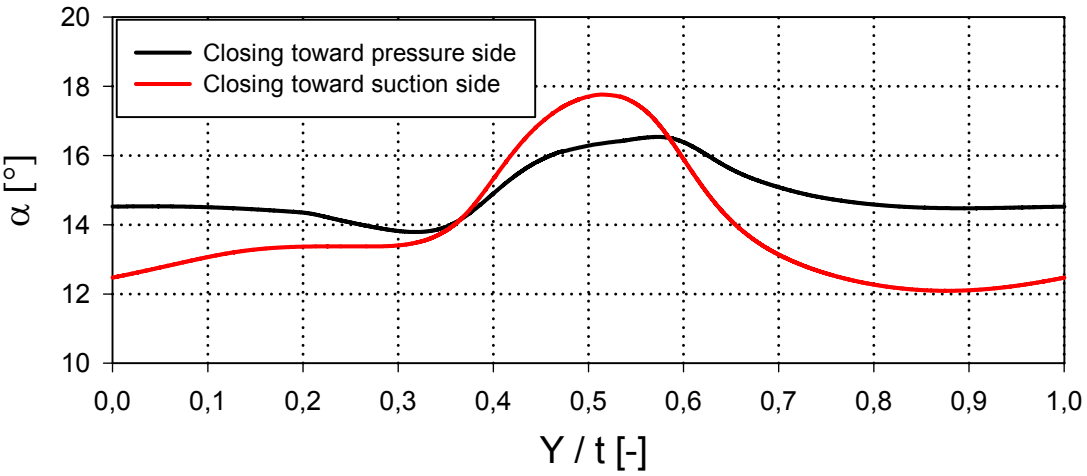

Figure 4.9: Pitchwise Flow Angle, 40% Closing toward Pressure Side and Suction Side, 6 *mm* Downstream of Trailing Edge

Figure 4.10 demonstrates that in 60% closing toward pressure side the pitchwise flow angle on the measurement line is almost constant (around 10°), while for closing toward suction side the maximum value occurs near the trailing edge ($Y/t = 0.5$).

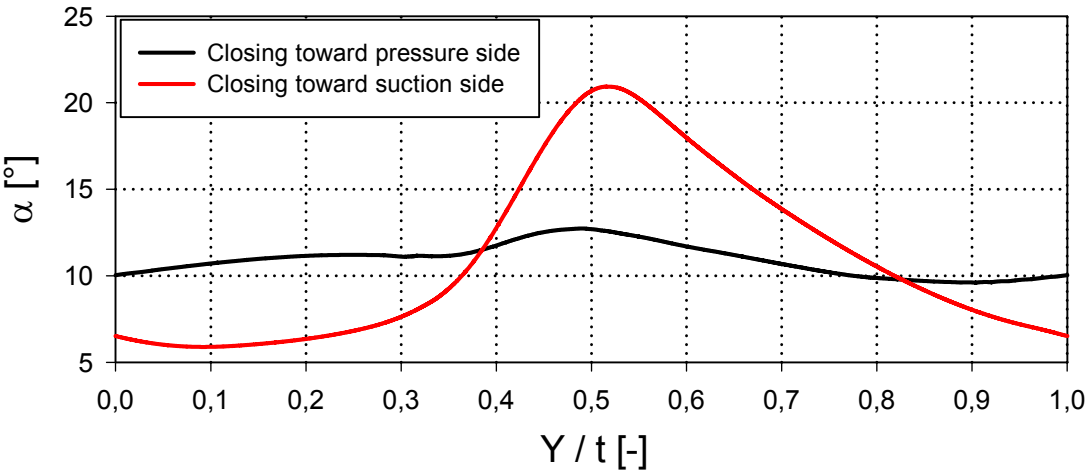

Figure 4.10: Pitchwise Flow Angle, 60% Closing toward Pressure Side and Suction Side, 6 *mm* Downstream of Trailing Edge

By comparing Fig. 4.6, 4.8, 4.9 and 4.10, it can be seen that with increase of closing degree, the pitchwise flow angle decreases. The reason could be that increasing the closing

degree results in separated flow and forms eddies along the suction side and pressure side. As it is witnessed, the separation on the pressure side for closing toward suction side, occupies a wider area than closing toward pressure side, hence the flow angle for closing toward suction side with the same closing degree is smaller than that for closing toward pressure side . As Fig. 4.11 illustrates forming of eddies impact on the main stream, i.e. the y-component of velocity (C_y) increases and according to Eq. 4.1, the flow angle decreases. The separation occurs in wider region through increasing the closing degree. Therefore, the pitchwise flow angle becomes lower.

In order to provide a better possibility of comparing flow angle (and other variable) and make the comparison more comprehensible, the mass averaged flow angle along the measurement line is applied

$$\overline{\alpha} = \frac{\int_{-t/2}^{t/2} \alpha\left(Y\right) \rho\left(Y\right) C\left(Y\right) \sin\left(\alpha\left(Y\right)\right) dY}{\int_{-t/2}^{t/2} \rho\left(Y\right) C\left(Y\right) \sin\left(\alpha\left(Y\right)\right) dY}. \tag{4.2}$$

Figure 4.13 shows the pitchwise mass averaged flow angle on the measurement line, 6 mm downstream of trailing edge. As mentioned above, it can be seen here that in both closing direction cases, with increasing the closing degree, the mass averaged flow angle decreases. The decrease of flow angle at low closing degrees, i.e. lower than 20%, has slight incline, while for higher closing degrees, higher than 20% the rate of decrease becomes steeper. Furthermore, it is apparent that closing toward pressure side shows greater value than closing toward suction side at the same closing degree, except when the closing degree is greater than ≈50%. This can be related to the flow angle near the trailing edge, which in the case of closing toward suction side is significantly greater than that for closing toward pressure side (Fig. 4.10). As mentioned above, the separation regions, on the pressure side or suction side of blade profile can affect the flow in main stream and form the flow. It is apparent that separation regions, in the case of closing toward suction side are considerably wider than that in the case of closing toward pressure side, particularly on the pressure side (Fig. 4.11b and 4.12b). Accordingly, it could be the reason of this significant difference in the flow angle near the trailing edge position, on the measurement line.

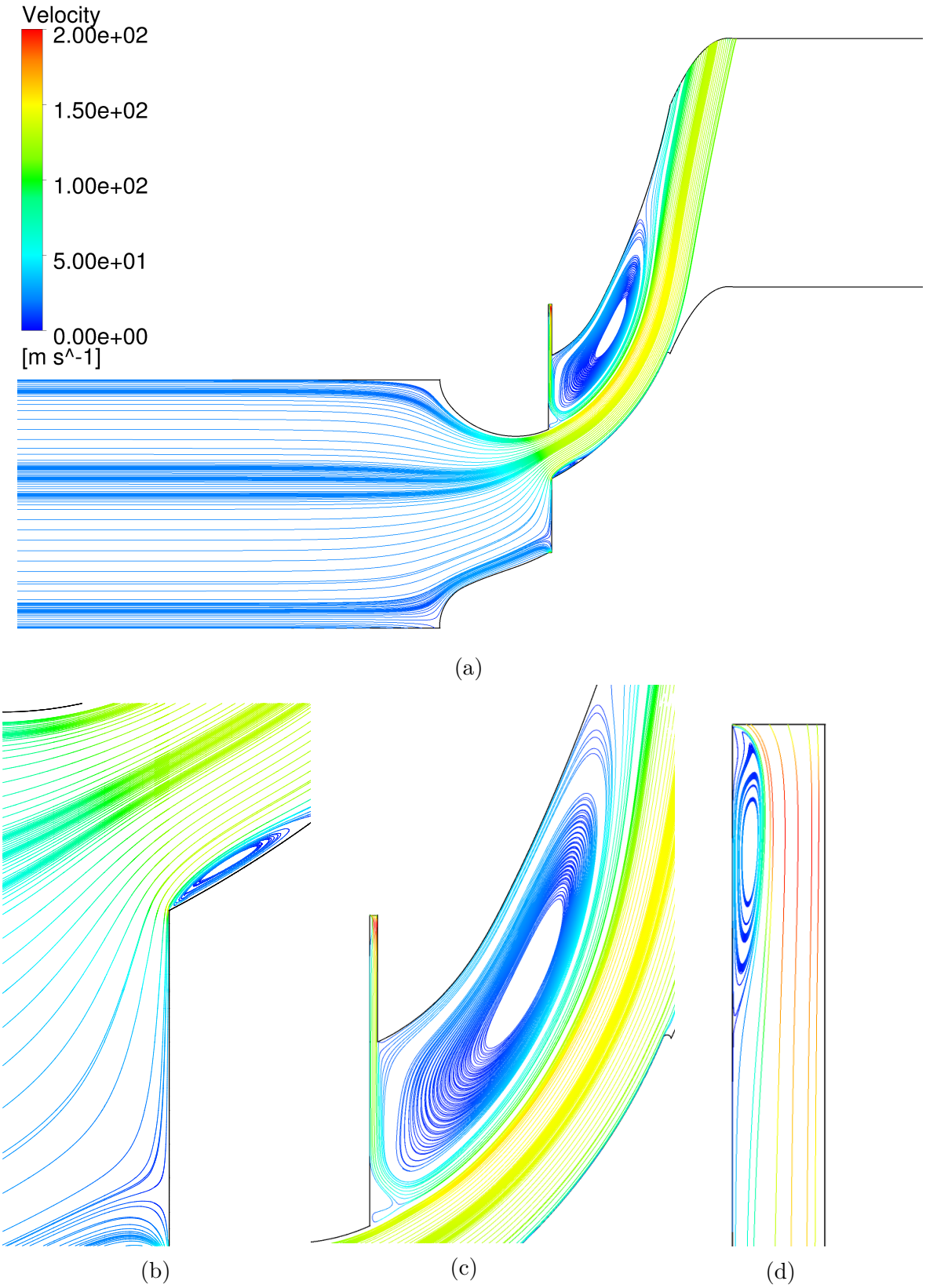

Figure 4.11: Streamline Patterns in the Flow Passage, 60% Closing toward Pressure Side

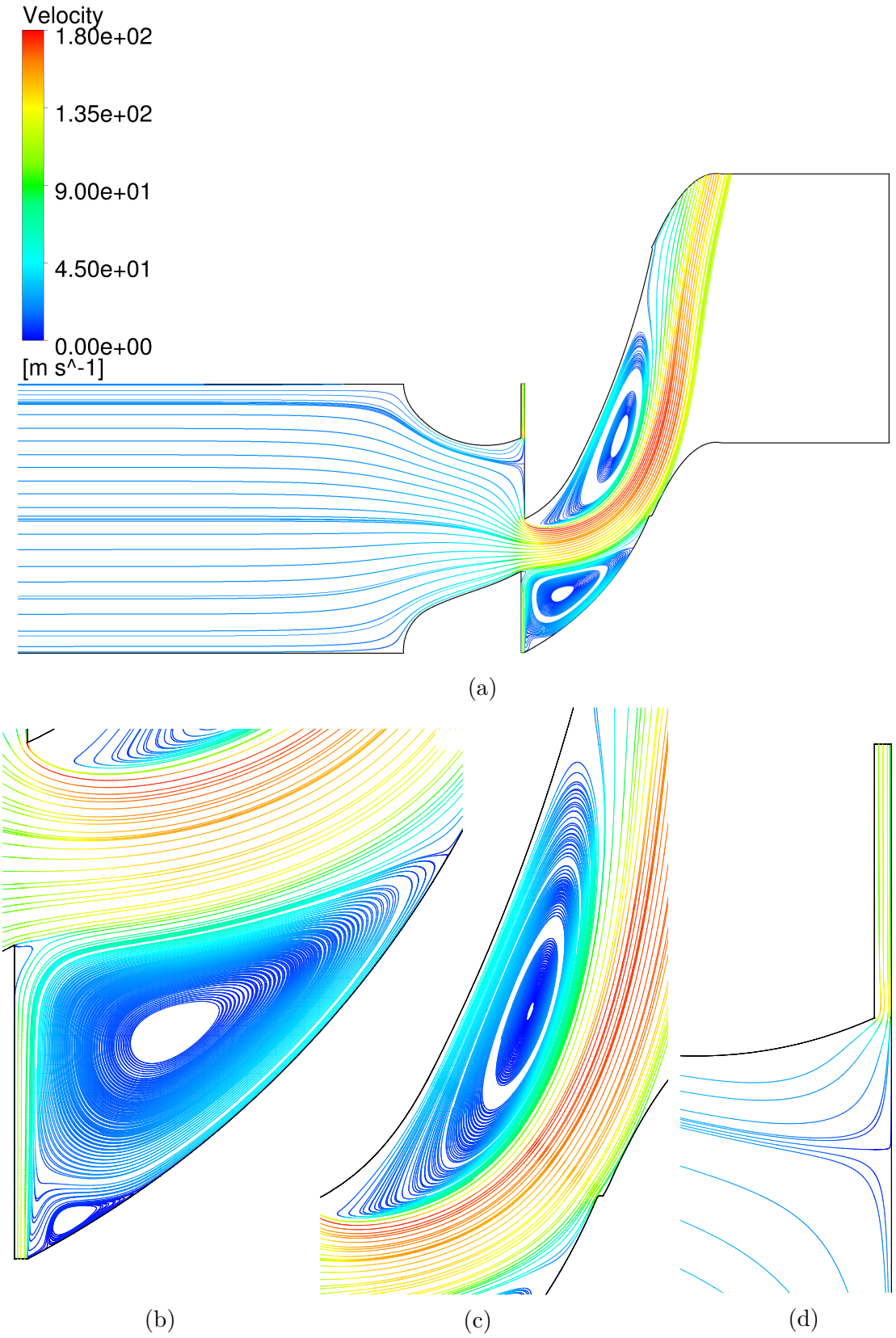

Figure 4.12: Streamline Patterns in the Flow Passage, 60% Closing toward Suction Side

Figures 4.11b and 4.12d reveal the location of second stagnation point on the edge of pressure side and edge of suction side. The issue of second stagnation point is discussed in detail in Sec. 4.4. It can be seen in Fig. 4.11d that the separation occurs in the gap in the case of closing toward pressure side. Besides the maximum velocity of the whole domain is formed here. Whereas, in the case of closing toward suction side the separation does not occur in the gap (Fig. 4.12d) and the maximum velocity arises in the main stream (Fig. 4.12c).

As stated above the mass averaged flow angle by closing degrees higher than 50% for closing toward suction side is greater than that of closing toward pressure side, which does not correspond to the experiment results of Kariman [9]. This unmatched result could be the consequence of the gap or numerical errors in CFD, caused by separation areas in respect to increase rate of turbulent and vortex generation. However, since there is not any experiment data available, real reason of this difference is not justifiable.

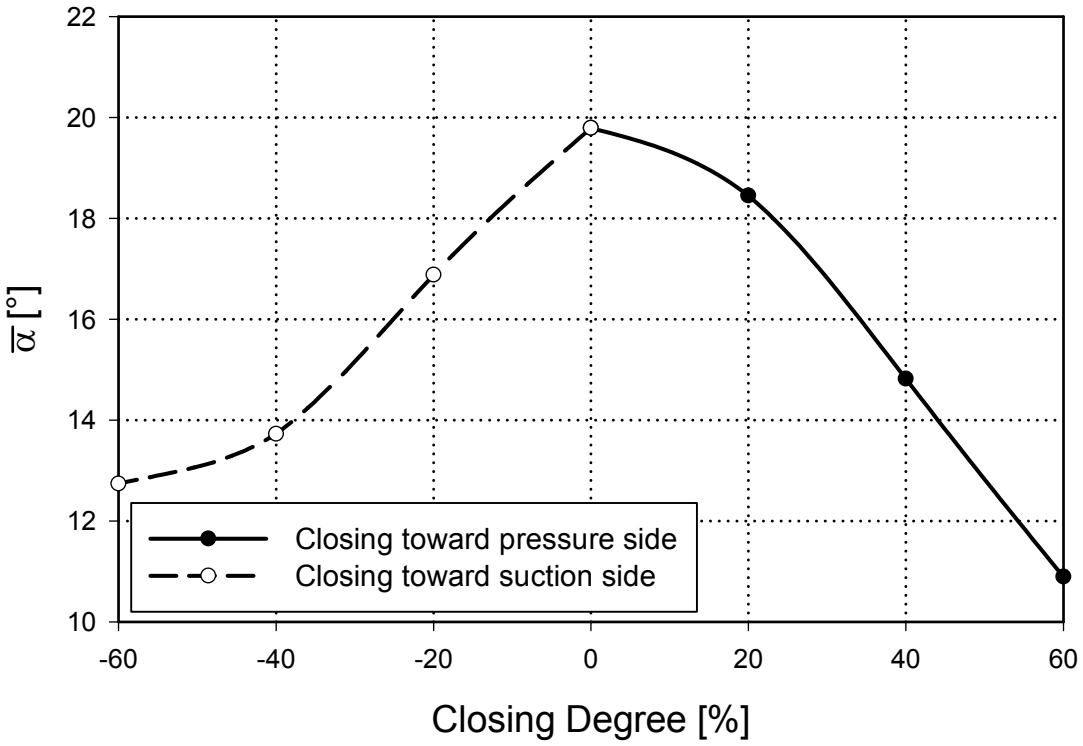

Figure 4.13: Mass Averaged Flow Angle for Closing toward Pressure Side and Suction Side

4.3 Static Pressure Coefficient

Static pressure coefficient (C_{ps}) can be defined as the static pressure difference between evaluated point and inflow, relative to dynamic pressure of inflow

$$C_{ps} = \frac{p - p_0}{\frac{1}{2}\rho_0 C_0^2}, \tag{4.3}$$

where p indicates the static pressure at the point in which pressure coefficient is being evaluated and subscript 0 indicates the variables at inlet. As mentioned above, it is assumed that flow is incompressible therefore, ρ_0 is constant.

Figure 4.14 illustrates the static pressure coefficient for a fully open case. It can be seen that the static pressure coefficient along the measurement line is almost constant and there is a slight increase at $Y/t = 0.4$. Comparing Fig. 4.14 with [9] shows good agreement in value of static pressure coefficient. The mass averaged static pressure coefficient is given by

$$\overline{C_{ps}} = \frac{\int_{-t/2}^{t/2} C_{ps}(Y)\,\rho(Y)\,C(Y)\sin(\alpha(Y))\,dY}{\int_{-t/2}^{t/2} \rho(Y)\,C(Y)\sin(\alpha(Y))\,dY},$$

which is equal to -8.96 and from experiment measured mass averaged static pressure coefficient is equal to -8.76 [9]. Figures 4.15, 4.16 and 4.17 demonstrate that with increasing the closing degree, the static pressure coefficient decreases. Furthermore, they display that C_{ps} is greater for closing toward pressure side than that for closing toward suction side at the same closing degree. It is evident that C_{ps} is not anymore almost constant at higher closing degrees for closing toward suction side, while it gets closer to quite constant for closing toward pressure side.

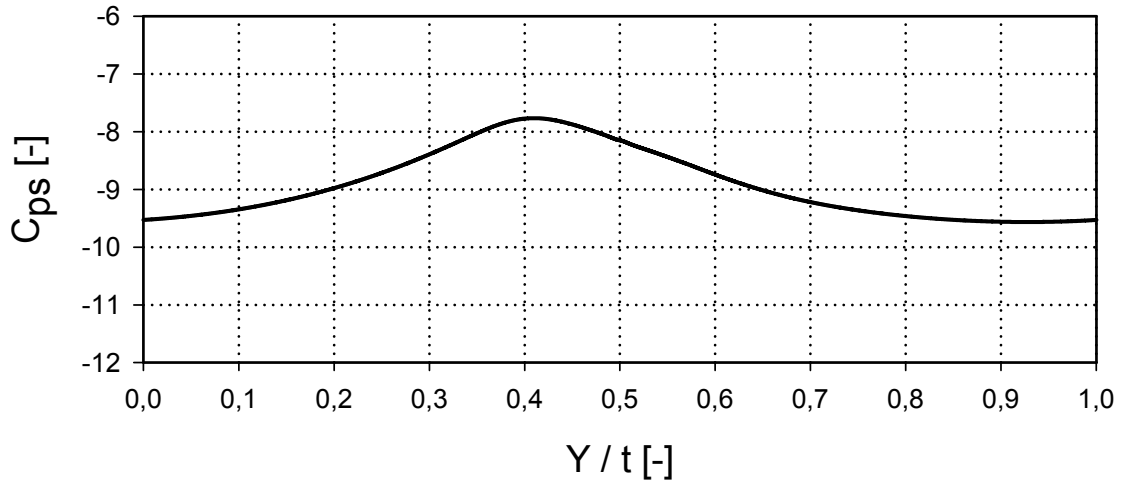

Figure 4.14: Pitchwise Static Pressure Coefficient, Fully Open, 6 mm Downstream of Trailing Edge

Figure 4.15 illustrates the pitchwise static pressure coefficient for 20% closing in both directions. It can be seen that the overall trend of this case is very similar to the fully open case. There is a maximum value of C_{ps} for both closing directions at $Y/t \approx 0.4$ as in fully open case.

Figure 4.16 reveals that C_{ps} has its maximum and minimum values respectively at $Y/t \approx 0.4$ and $Y/t \approx 0.72$. By increasing of closing degree (Fig. 4.17), the deviation of C_{ps} becomes stronger for closing toward suction side in the range of $Y/t \approx 0.4$ to 0.8.

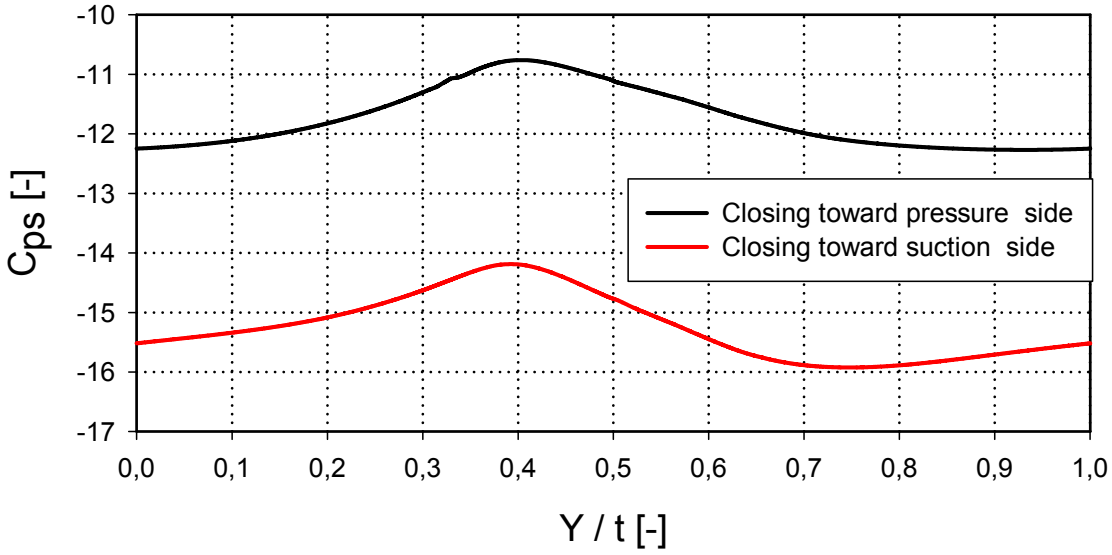

Figure 4.15: Pitchwise Static Pressure Coefficient, 20% Closing toward Pressure Side and Suction Side, 6 mm Downstream of Trailing Edge

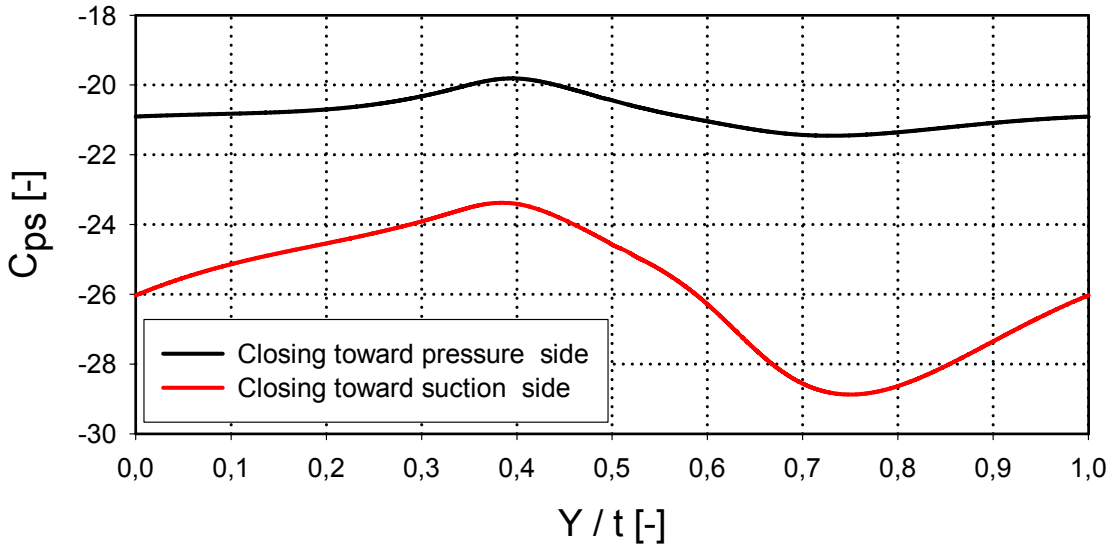

Figure 4.16: Pitchwise Static Pressure Coefficient, 40% Closing toward Pressure Side and Suction Side, 6 mm Downstream of Trailing Edge

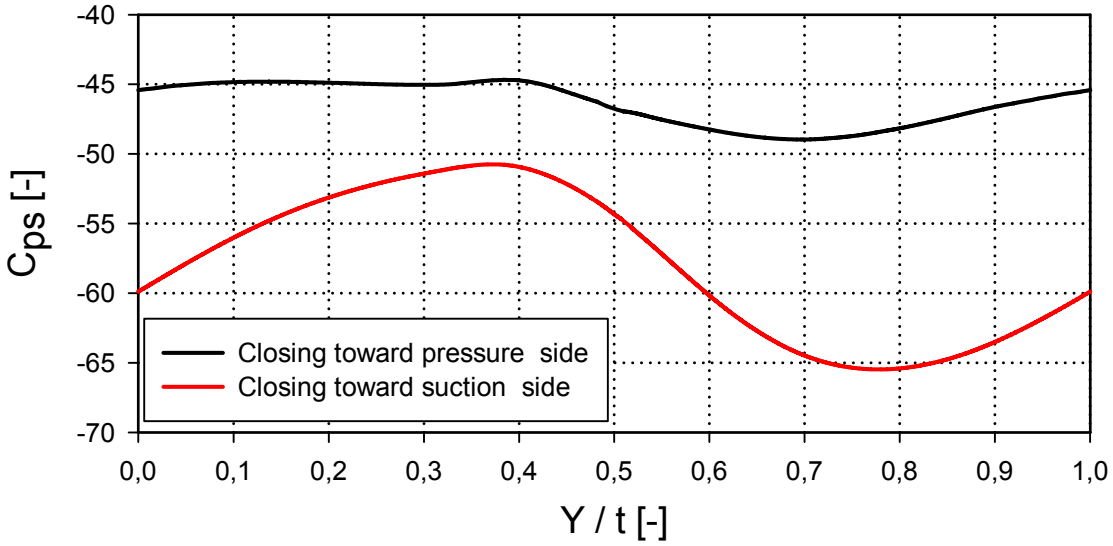

Figure 4.17: Pitchwise Static Pressure Coefficient, 60% Closing toward Pressure Side and Suction Side, 6 mm Downstream of Trailing Edge

Table 4.1 shows the mass averaged C_{ps} of different closing degrees in both directions. It can be seen that through increasing the closing degree, the mass averaged static pressure decreases. It is apparent the decreasing rate of the closing toward the suction side is faster than that of closing toward pressure side.

	Closing toward Pressure Side	Closing toward Suction Side
20%	-11.8	-15.3
40%	-20.8	-25.8
60%	-46.2	-59.6

Table 4.1: Mass Averaged Static Pressure Coefficient for Closing toward Pressure Side and Suction Side, 6 mm Downstream of Trailing Edge

4.4 Static Pressure Coefficient Distributions on Blade Surfaces

In this section distribution of static pressure coefficient on the blade surfaces, i.e. on the pressure side and suction side for different closing degrees is presented. In order to

make the x-axis dimensionless, it is divided by axial chord length ($b = 74.05\ mm$). As mentioned in Sec. 3.3.1, the gap is located at 0.486<x (mm)<1.486, which can be seen at $X/b \approx 0.5$.

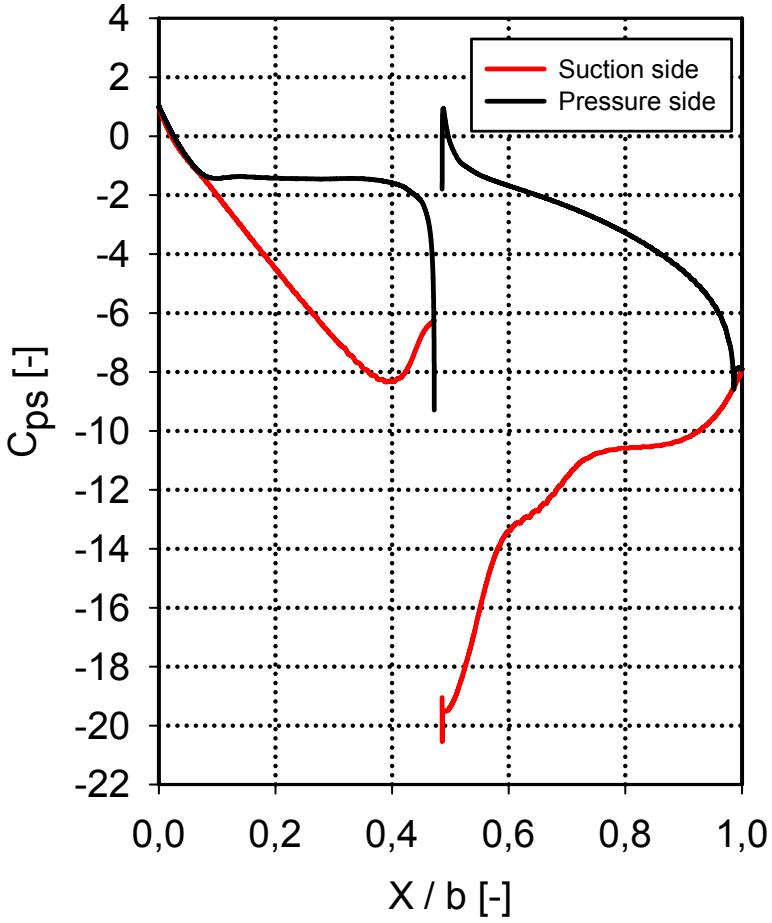

Figure 4.18: Static Pressure Coefficient Distribution on Blade Surfaces, Fully Open

Figure 4.18 indicates the maximum static pressure coefficient equal to 1 at leading edge ($X/b = 0$), which shows that the stagnation point is located here. It can be seen that static pressure coefficient decreases on the pressure side of blade between $X/b = 0$ and 0.1. In other word, the flow is accelerated in this range. After that the static pressure coefficient remained almost constant between $X/b = 0.1$ and ≈0.4. It is apparent that the static pressure coefficient changes significantly in the gap region ($X/b \approx 0.5$). It can be seen that on the left side of the gap, C_{ps} drops. This sudden reduction of C_{ps} can be the consequence of separated flow on the left wall of the gap. On the right side of the gap there is a jump of C_{ps} on pressure side. After this sudden increase C_{ps} reaches its maximum value again, which indicate another stagnation point on the pressure side just after the gap. It can be observed on the suction side that C_{ps} decreases between

$X/t = 0$ and ≈ 0.4 (maximum velocity in vicinity of blade suction side of moving part). Afterwards, it begins to increase till it reaches the gap, which shows the deceleration of flow. It is evident that C_{ps} falls down suddenly after the gap, due to the separated flow on the suction side in this point, which is the consequence of flow through the gap from pressure side to suction side. After that C_{ps} increases again up to trailing edge ($X/b = 1$). The deceleration of flow on the suction side can affect the boundary layer and can be the reason of separation. According to *Traupel* concerning a blade profile [24] if

$$\sqrt{\frac{1 - C_{ps,min}}{1 - C_{ps}}} > 1.4, \tag{4.4}$$

then separation can occur on the suction side. Where C_{ps} is the static pressure Coefficient at the trailing edge ($X/b = 1$).

Figure 4.19 illustrates the distribution of static pressure coefficient for 20% closing in both directions. Similar to fully open case, stagnation point can be seen at leading edge in both cases. In terms of closing toward pressure side, C_{ps} on pressure side is almost constant up to the gap, while it is decreasing on the suction side. The jump of C_{ps} after the gap indicates the second stagnation point, which places on the edge of pressure side (Fig. 3.16b, Boundary No:10). Afterwards, C_{ps} increases to -5, which can be the reason of local separation at this location.

It can be seen for closing toward suction side that C_{ps} on the suction side is greater than that on the pressure side, at moving part, i.e. near the leading edge and near the gap. Opposite closing toward pressure side, for closing toward suction side the second stagnation point occurs on the edge of suction side (Fig. 3.16c, Boundary No:9), regarding the jump of C_{ps} to 1 in this location. Figure 4.20 illustrates the contour of C_{ps} in computational domain. The location of second stagnation point is clearly apparent on the edge of pressure side (for closing toward pressure side) and on the edge of suction side (for closing toward suction side). Figure 4.20 visualizes also the separation regions, which have very low C_{ps} (regions with blue color) comparing to main stream flow and not separated flow regions.

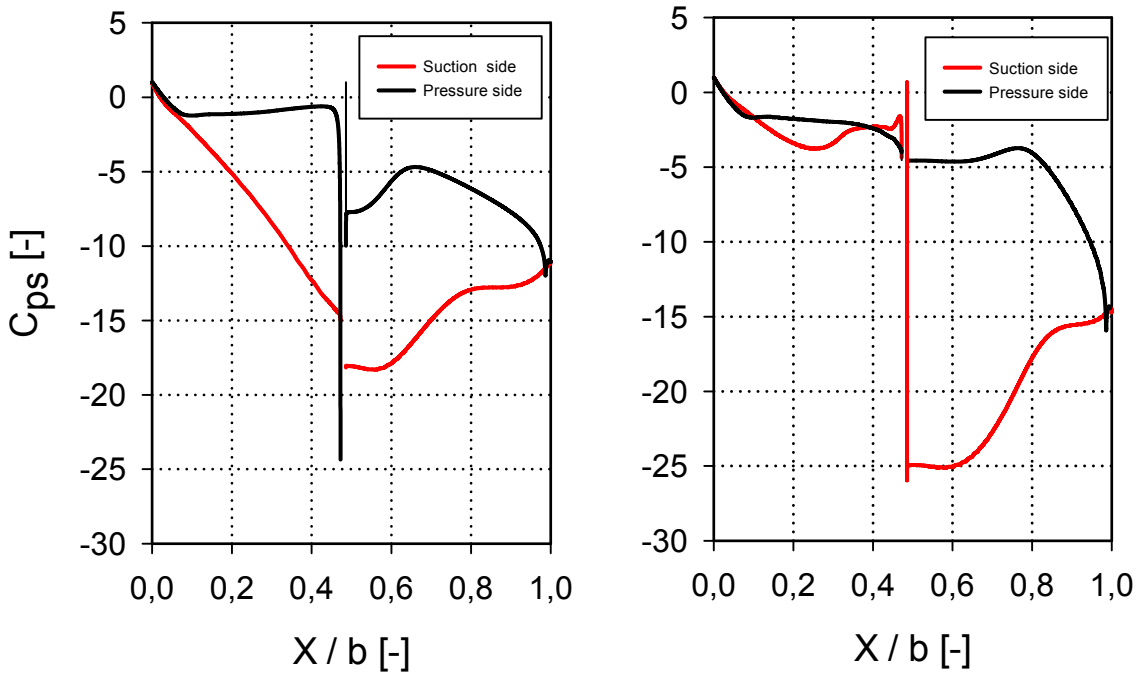

(a) Closing toward Pressure Side (b) Closing toward Suction Side

Figure 4.19: Static Pressure Coefficient Distribution on Blade Surfaces, 20% Closing Degree

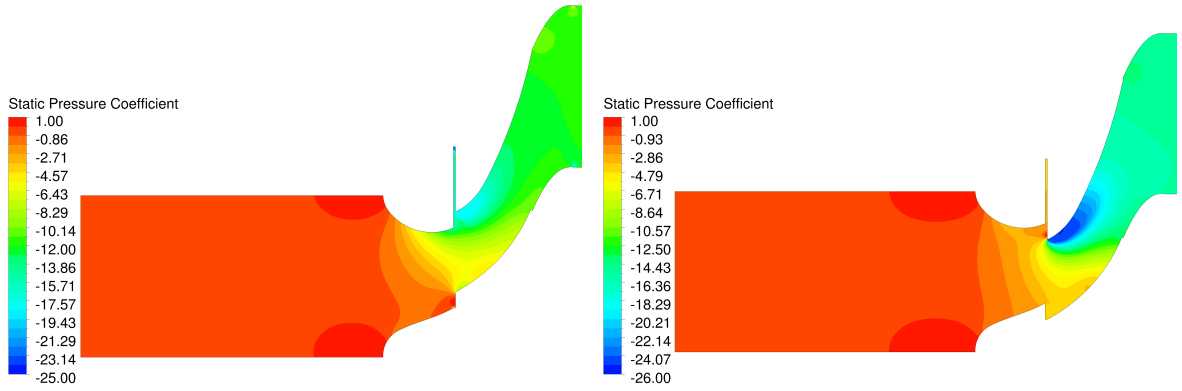

(a) Closing toward Pressure Side (b) Closing toward Suction Side

Figure 4.20: Contour of Static Pressure Coefficient, 20% Closing Degree

By comparing Fig. 4.19, 4.21 and 4.22, it can be recognized that with increasing the closing degree, the difference of C_{ps} between pressure side and suction side in the moving

part increases, while this difference on the fix part ($X/b > 0.5$) is more or less constant. On the other hand, in terms of closing toward suction side, it can be seen that with increasing the closing degree, C_{ps} on the suction side transcends the one on the pressure side, which results in a reverse flow from suction side to pressure side of blade through the gap (discussed in Sec. 4.7).

It is apparent that with increasing the closing degree in both closing directions, the minimum C_{ps} which is located on the suction side of fix part decreases. This could be the consequence of separated region, that becomes greater by higher closing degree.

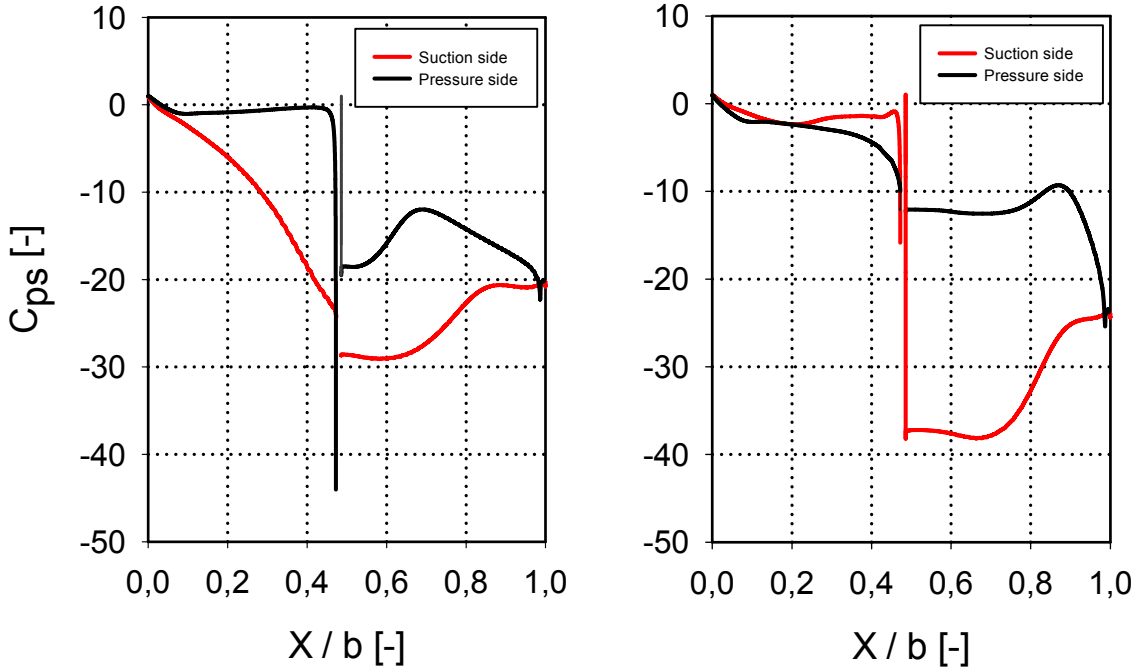

(a) Closing toward Pressure Side

(b) Closing toward Suction Side

Figure 4.21: Static Pressure Coefficient Distribution on Blade Surfaces, 40% Closing Degree

It can be seen that through increasing the closing degree the level difference of C_{ps} between fix part and moving part increases. This can be caused by greater separated flow region, as well as higher magnitude of velocity, because of constriction of cross section between moving part and fix part while the volume flow rate at the inlet is constant.

This point should be considered that for closing toward suction side, the difference of

C_{ps} between pressure side and suction side of fixed part is greater than that of closing toward pressure side. Greater difference between pressure side and suction side normally leads to smaller flow angle (correspond with the results in Sec. 4.2)

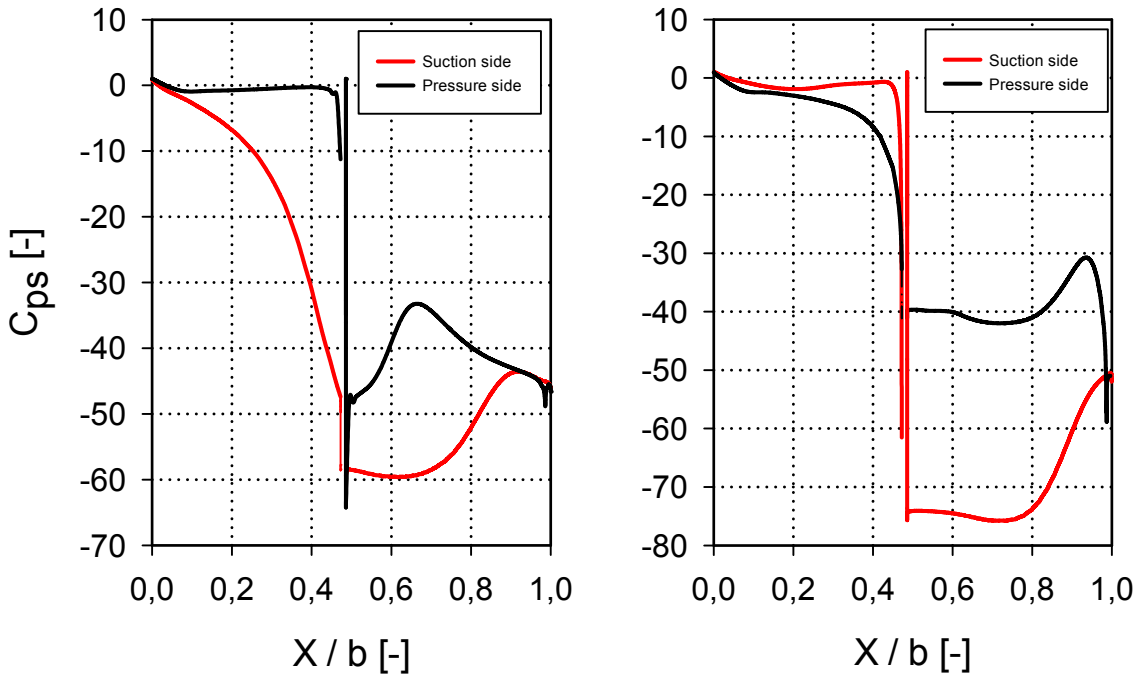

(a) Closing toward Pressure Side

(b) Closing toward Suction Side

Figure 4.22: Static Pressure Coefficient Distribution on Blade Surfaces, 60% Closing Degree

4.5 Total Pressure Coefficient

Total pressure could be considered principally as the sum of static pressure and dynamic pressure

$$p_t = p + \frac{1}{2}\rho C^2.$$

In order to quantify the flow losses in turbine blades cascades total pressure coefficient (C_{pt}) can be used. This factor indicates the total pressure difference between the undisturbed inflow (normally inlet) and the measuring position relative to the dynamic pressure of the undisturbed inflow. Total pressure coefficient is

$$C_{pt} = \frac{p_t - p_{t0}}{\frac{1}{2}\rho_0 C_0^2}, \tag{4.5}$$

where p_t indicates total pressure at the point in which pressure coefficient is being evaluated and subscript 0 indicates the variables at inlet.

Figure 4.23 illustrates the C_{pt} on the measurement line 6 mm downstream of trailing edge. This figure indicates decreasing of the C_{pt} within the wake region ($0.4 < Y/t < 0.6$), in other word increasing the losses in this region. By way of explanation, in the wake region, velocity decreases. It means decline of dynamic pressure and decreasing of total pressure. It can be seen that in inviscid flow region C_{pt} is constant and approximately equal to zero, which shows very small losses in this region. Furthermore, it is apparent that the trend of total pressure coefficient is almost symmetry, which shows the equally development of boundary layer from both pressure side and suction side up to downstream of trailing edge (on the measurement line).

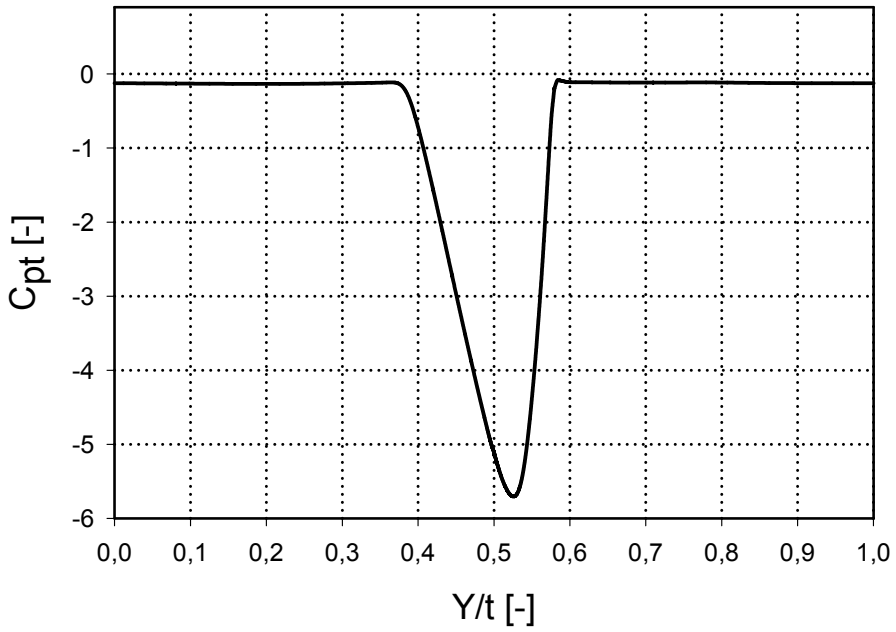

Figure 4.23: Pitchwise Total Pressure Coefficients, Fully Open, 6 *mm* Downstream of Trailing Edge

Increasing the closing degree to 20% (Fig. 4.24) indicates increment of width of wake region particularly for closing toward suction side as well as decrease of minimum of C_{pt}. It signifies greater loses in wake region, which can be the consequence of formation of separated flow and vortices. It is noticeable that the wake region for closing toward suctions side is wider than that of closing toward pressure side. likewise, the minimum of C_{pt} is lower, which can be the influence of stronger flow blockage and formation of flow vortices downstream of the backward facing step in this case. Figures 4.25 and 4.26 show that separated flow concerning closing toward suction side is significantly greater than that of closing toward pressure side, particularly on the pressure side of blade cascade. This can result in blockage of flow, higher turbulent generation and consequently decrease in C_{pt} and increase in losses.

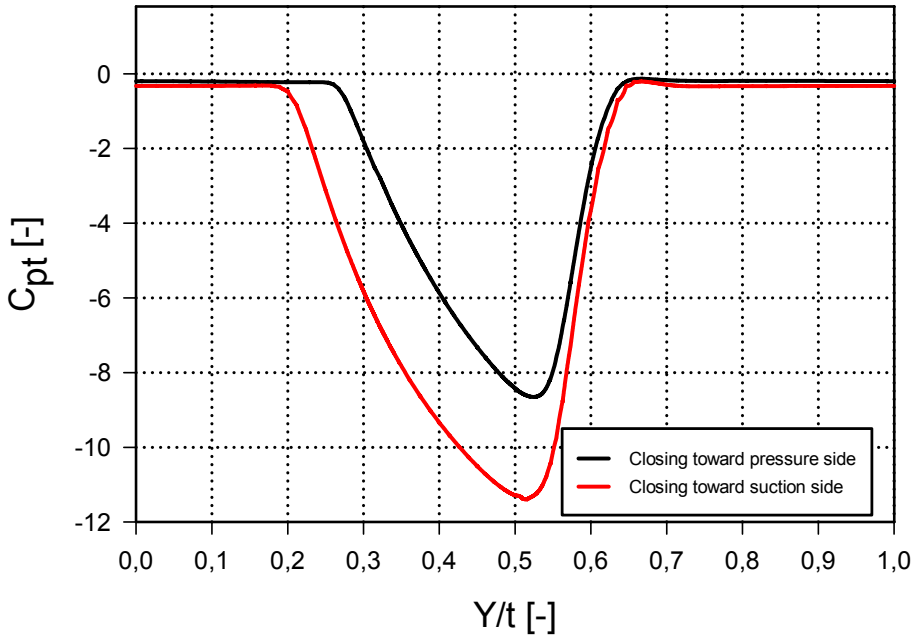

Figure 4.24: Pitchwise Total Pressure Coefficient, 20% Closing toward Pressure Side and Suction Side, 6 *mm* Downstream of Trailing Edge

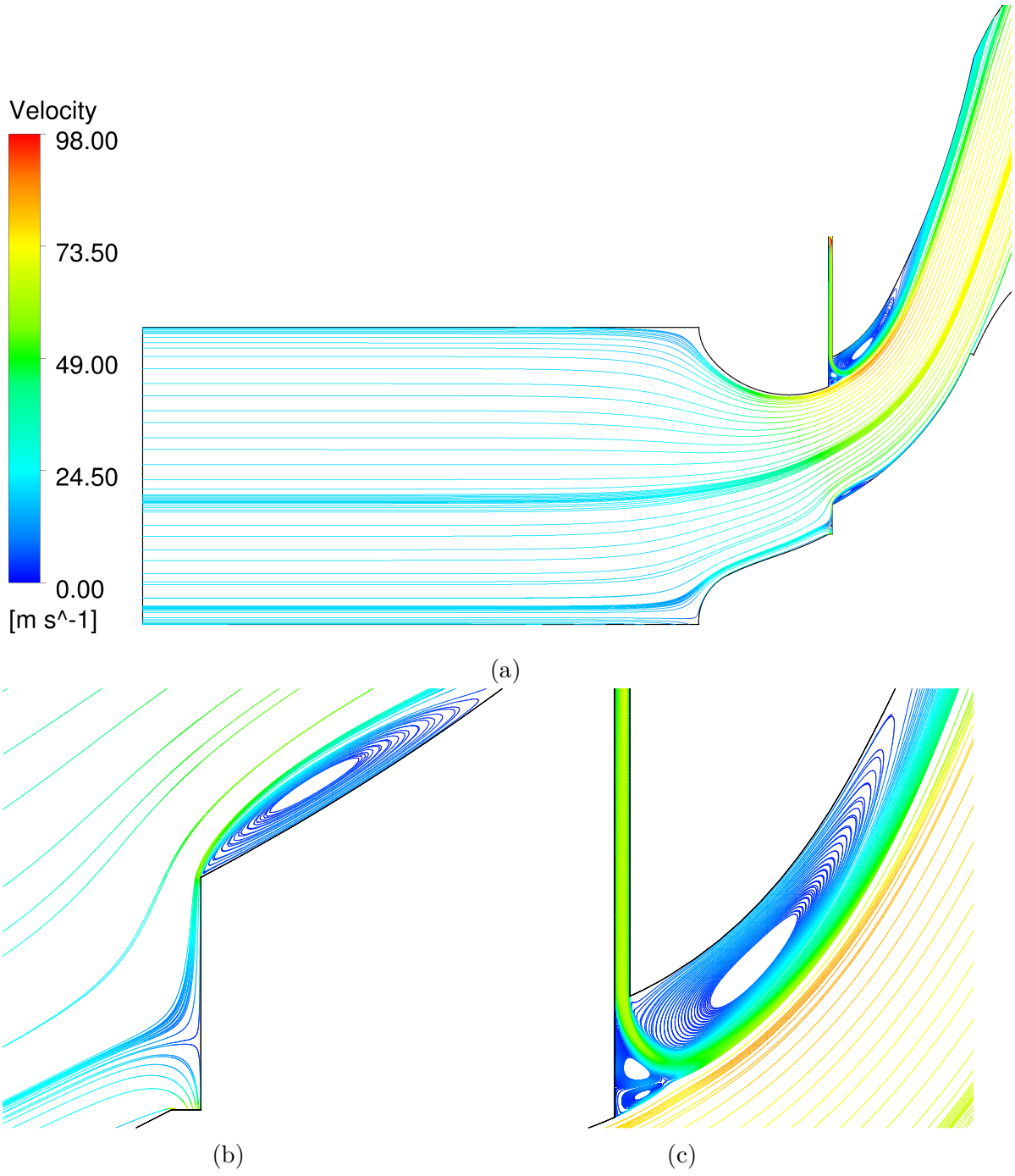

Figure 4.25: Streamline Patterns in the Flow Passage, 20% Closing toward Pressure Side

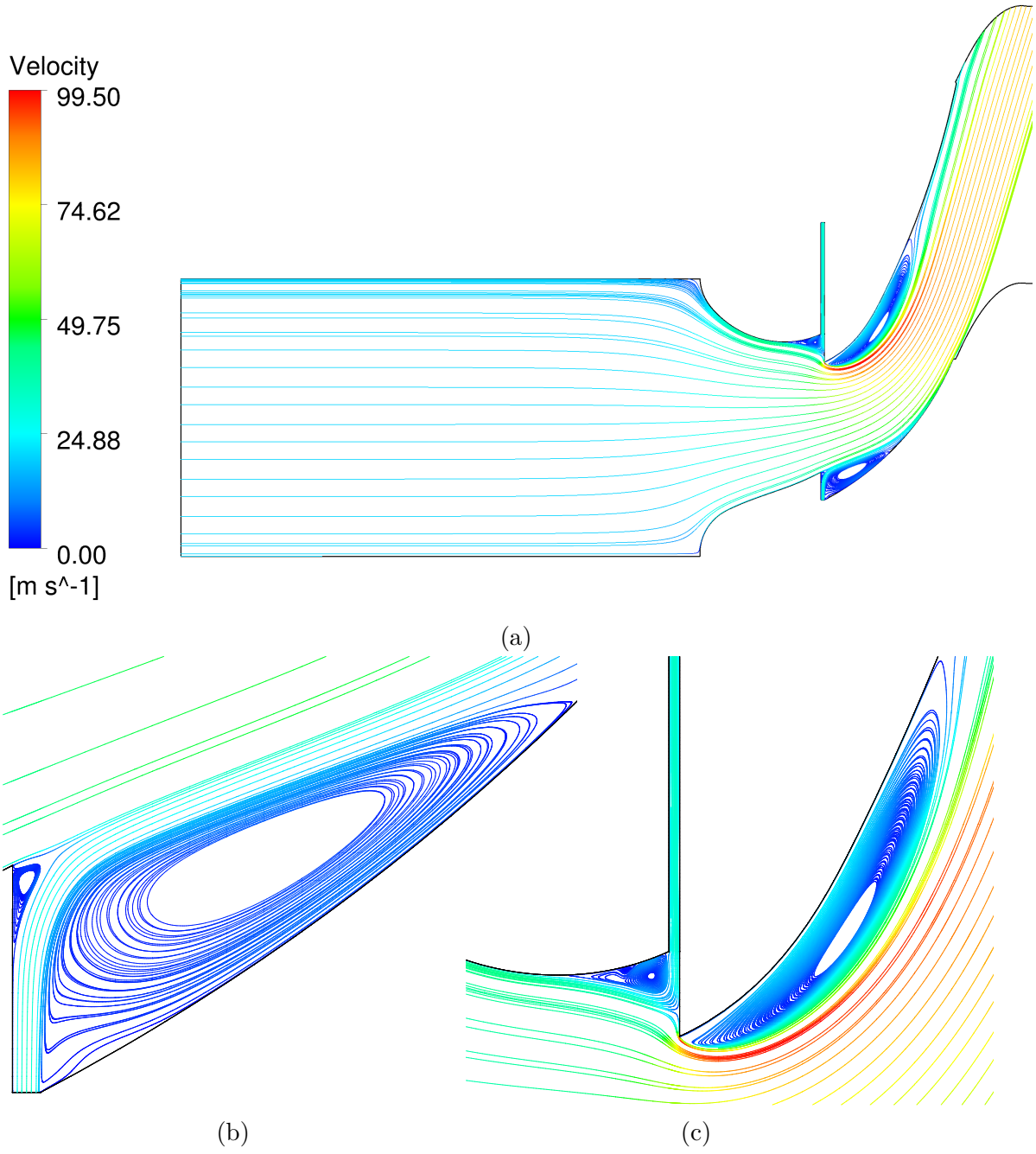

Figure 4.26: Streamline Patterns in the Flow Passage, 20% Closing toward Suction Side

Comparing Fig. 4.24 and 4.27 indicates that by increasing the closing degree from 20% to 40%, the width of inviscid region of pressure side does not change significantly. Although the minimum values of C_{pt} decreases which can be considered as decreasing of the velocity around the wake region and its effect on the flow dynamic pressure as a portion of total

pressure.

On the other hand, concerning closing toward suction side, changes in inviscid region are more obvious. Furthermore, it is evident that the distribution of C_{pt} is asymmetric, and it can be as a reason of not uniform development of boundary layer on suction side and pressure side.

Figure 4.28 demonstrates that in higher closing degree (60%), total pressure coefficient changes significantly for both closing directions. It is witnessed that in both cases (closing toward pressure side and suction side) the inviscid region is eliminated. The value of C_{pt} deviates from zero in the regions far from trailing edge, i.e. $Y/t < 0.2$ and $Y/t > 0.8$, though still the value of C_{pt} is closer to zero in comparison to regions near the trailing edge. Minimum value of C_{pt} for closing toward pressure side is greater than that of closing toward suction side (similar to other closing degrees). Furthermore, it is significant that the distribution of C_{pt} is not symmetric in both closing direction cases, which is more noticeable for closing toward suction side. This result could be consequence of greater separated flow and vortices in comparison to closing toward pressure side (Fig. 4.11 and 4.12), which affect the boundary layer.

It should be noted that in high closing degrees velocity gradients, formation of vortices and turbulent generation are higher than in low closing degree cases. Hence the CFD errors should be taken into account.

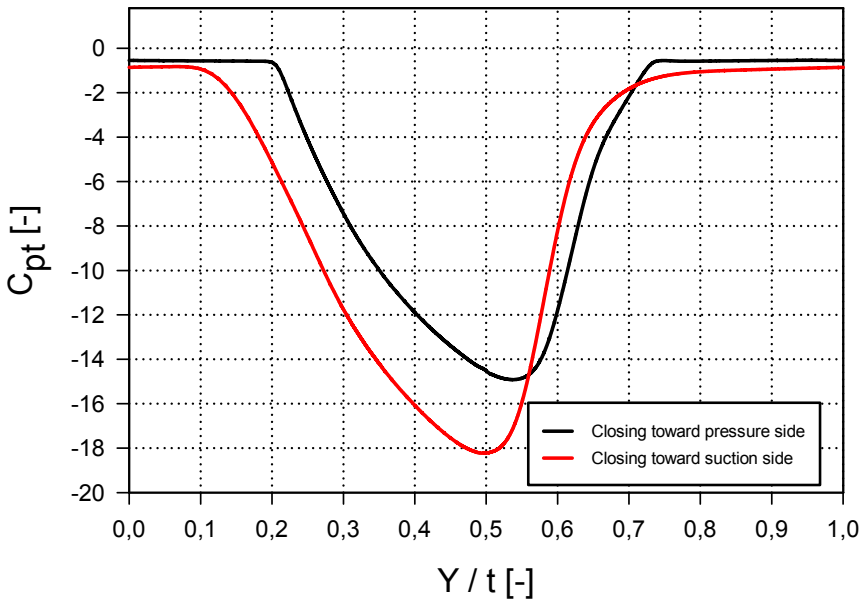

Figure 4.27: Pitchwise Total Pressure Coefficient, 40% Closing toward Pressure Side and Suction Side, 6 *mm* Downstream of Trailing Edge

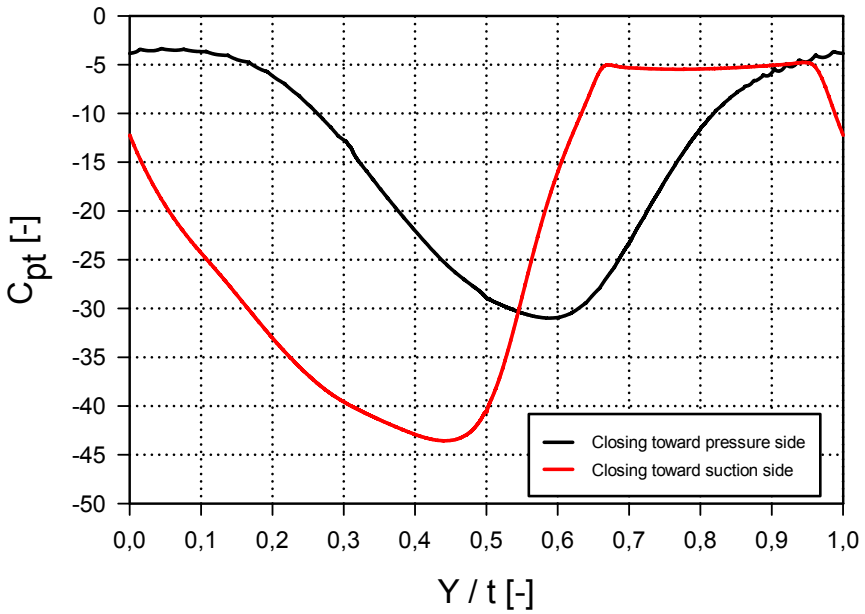

Figure 4.28: Pitchwise Total Pressure Coefficient, 60% Closing toward Pressure Side and Suction Side, 6 *mm* Downstream of Trailing Edge

As discussed above, the pitchwise mass averaged parameters provide a better comparison of a variable for different closing degrees. Pitchwise mass averaged total pressure coefficient is calculated as

$$\overline{C}_{pt} = \frac{\int_{-t/2}^{t/2} C_{pt}(Y)\,\rho(Y)\,C(Y)\sin(\alpha(Y))\,dY}{\int_{-t/2}^{t/2} \rho(Y)\,C(Y)\sin(\alpha(Y))\,dY}. \tag{4.6}$$

Figure 4.29 illustrates the pitchwise mass averaged total pressure coefficient in both closing directions for different closing degrees. As mentioned above, it can be seen that $\overline{C}_{pt}$ for closing toward suction side is lower than that of closing toward pressure side. It is clear that there is a slight variance of $\overline{C}_{pt}$ in low closing degrees between closing toward pressure side and closing toward suction side, which increases significantly in high closing degrees. Furthermore, this point should be taken into consideration that variation of $\overline{C}_{pt}$ from 40% to 60% is conspicuously greater than that between lower closing degrees. This issue can be judged for rapidly escalation of losses in high closing degrees, in terms of large separated flow regions and heavier blockage of the flow.

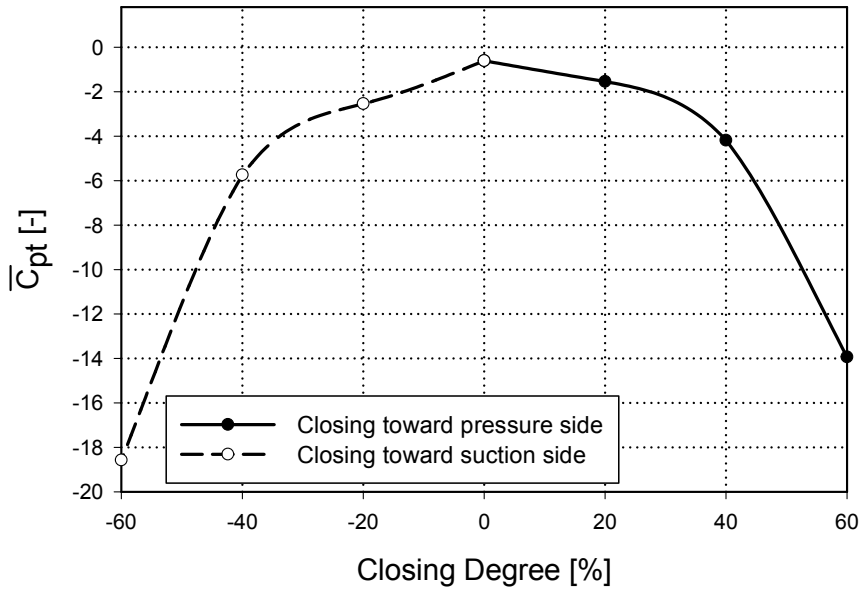

Figure 4.29: Mass Averaged Total Pressure Coefficient for Closing toward Pressure Side and Suction Side, 6 mm Downstream of Trailing Edge

Figure 4.29 shows that closing toward pressure side is predominantly advantageous to closing toward suction side, particularly for higher closing degrees, as the total pressure

coefficient is an important factor to measure the loss in downstream of the flow over the blade, which is discussed in the next section.

4.6 Loss Coefficient

Loss coefficient can be calculated through

$$\zeta = -\overline{C}_{pt} \left(\frac{\sin \overline{\alpha}}{\sin \overline{\alpha_0}} \right)^2, \tag{4.7}$$

where $\overline{C}_{pt}$ is pitchwise mass averaged total pressure coefficient, $\overline{\alpha}$ is pitchwise mass averaged flow angle and $\overline{\alpha_0}$ is inflow angle, which is replaced for 90° in this work.

The calculated loss coefficients in both directions are plotted in Fig. 4.30 for different closing degrees. It can be witnessed clearly that with increasing the closing degree in both closing directions, the loss coefficient increases. It is well recognized in this figure that the loss coefficient for closing toward pressure side is significantly smaller than that of closing toward suction side, specially for closing degrees higher than 40%.

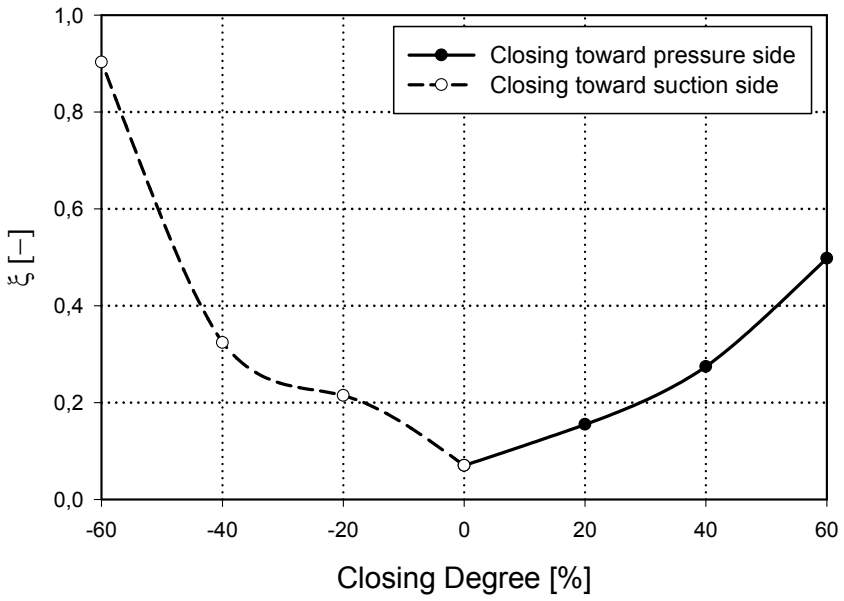

Figure 4.30: Loss Coefficient for Closing toward Pressure Side and Suction Side, 6 *mm* Downstream of Trailing Edge

Figure 4.30 indicates again that closing toward pressure side has the advantage of lower loss coefficient in comparison to closing toward suction side, though there is a slight difference in lower closing degrees, i.e closing degrees smaller than 40%.

4.7 Volume Flow Rate through the Gap

In order to investigate the impact of closing degree on the flow through the gap, the normalized volume flow rate is calculated by

$$\frac{Q}{Q_0} = \frac{\overline{C_g} A_g}{\overline{C_0} A_0},$$

where $\overline{C_g}$ is the averaged velocity at the inlet of the gap, A_G is the surface of the gap (Fig. 3.16 boundary No:5) and Q_0 is the volume flow rate at the inlet.

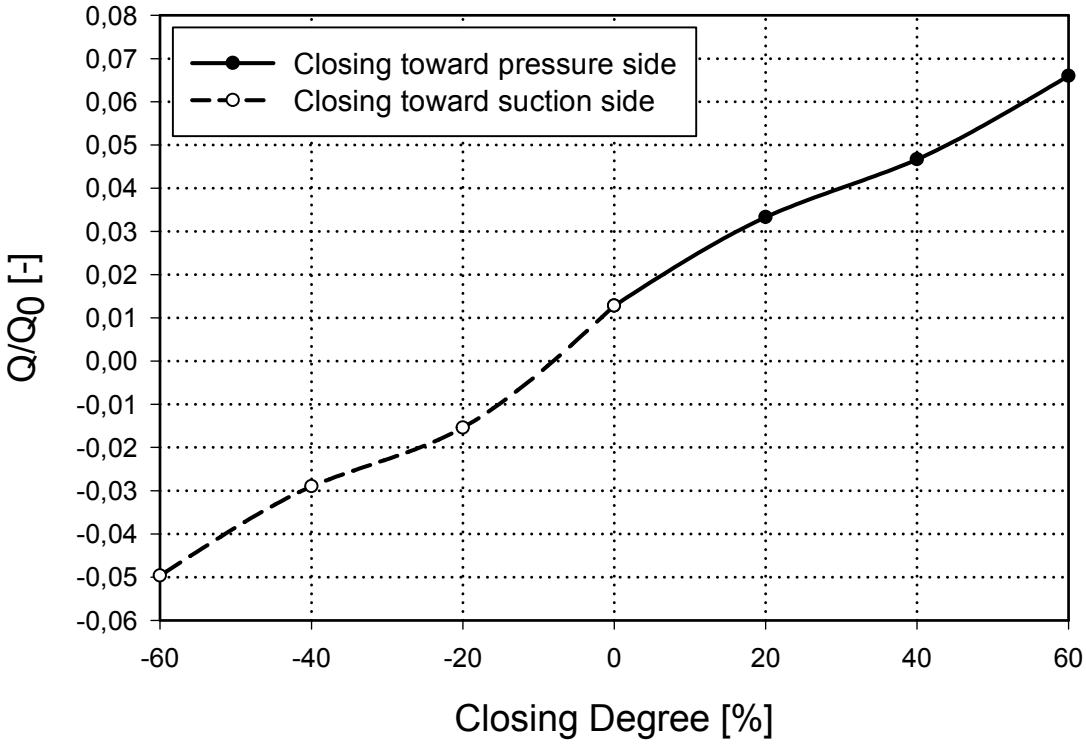

Figure 4.31: Normalized Volume Flow Rate Through the Gap for Closing toward Pressure Side and Suction Side

It is evident that by increasing the closing degree, the volume flow rate increases as well, which is between ≈1 to 7% of inflow for closing toward pressure side and ≈1 to 5% of inflow for closing toward suction side. It is obvious that Q/Q_0 for closing toward pressure side is greater than that of closing toward suction side. This shows that pressure gradient between pressure and suction sides of blade is greater, which can be seen in Sec. 4.4 as well. It is considerable that the value of Q/Q_0 for closing toward suction side is negative, i.e. for closing degrees greater than ≈ 10%. This shows that flow through the gap is in opposite direction, i.e. from suction side to pressure side of blade cascade. This means that the static pressure on the suction side should be greater than that on pressure side of blade. This issue is discussed in Sec. 4.4 and can be observed in Fig. 4.20b, 4.21b and 4.22b on the moving part of blade ($Y/t < 0.5$). It is apparent in Fig. 4.20b that the static pressure on the suction side only near the trailing edge and near the cutting line position is greater, while with increasing the closing degree the static pressure on the whole moving part of suction side ($0 < Y/t < 0.5$) becomes greater than that on pressure side. Furthermore, pressure gradient between suction and pressure sides of blade cascade elevates with increasing the closing degree toward suction side. This results in higher volume flow rate through the gap.

It is noteworthy to mention that volume flow rate is equal to zero in case of closing toward suction side for closing degree around 10%, which means that in this case the static pressures on the suction side and pressure side of moving part are equal.

5 Conclusion

In this work different types of extraction steam turbine, such as condensing extraction steam turbine and back-pressure extraction steam turbine, as well as the various types of controlling mechanism of steam extraction has been reviewed. It has been shown that using throttling valves causes high flow loss. Therefore, using rotary valve as nozzle blades cascade in low pressure stage of the turbine, can be reasonable. For this purpose T100 blade profile with 80 mm pitch length is selected. Since a rotary valve is applied in the industrial application, which uses a needle roller bearing to reduce the friction of a rotating surface, an axial gap between fix part and moving part of blade profile has been taken into consideration.

In order to investigate the flow characteristics, the numerical solution has been applied. The high *Reynolds* number, i.e. 4.15×10^5, indicates the turbulent flow in computational domain. Therefore, RANS equations are used to describe the turbulent flow. For this reason, different turbulence models have been compared with each other. It has been shown that SST $k-\omega$ model employs the strength of both $k-\omega$ and $k-\epsilon$ models and puts aside their weaknesses.

For the purpose of CFD investigation, different positions of blades cascade, depending on closing degree of rotary valve, i.e. fully open, 20%, 40% and 60% closing of blades cascade, toward pressure and suction sides are created.

The structured mesh is generated, which increase the ability of controlling the size of cells in critical regions such as in vicinity of blade surfaces (walls), leading edge and trailing edge. The value of y^+ in different cases has been investigated. This shows the accuracy of the results in the boundary layer near the walls. It has been shown that during an iterative process of mesh generation, y^+ is held under five to make sure that the first cell is within the viscous sublayer region. Afterwards the mesh quality criterion has been investigated to ensure the high accuracy of CFD results.

The flow characteristics such as flow velocity, flow angle, static and total pressure coefficient and loss coefficient have been investigated during the post-processing on the measurement line, 6 mm downstream of trailing edge. It has been indicated that with increasing the closing degree the wake region spreads specially at higher closing degrees, which widened the wake region to the whole pitchwise length on measurement line. This action results in higher loss coefficient in comparison to lower closing degrees.

It has been demonstrated that closing toward pressure side is generally more efficient than closing to suction side, due to wider separation area, which results in formation of stronger vortices and blockage of the flow passage.

It is observed that air flows from suction side to pressure side, when closing degree toward suction side is greater than $\approx 10\%$.

In terms of future works, some proposals could be recommended such as: experimental measurement of 2D rotary valve, studying the effect of gap with different axial lengths, Investigating in 3D case (numerical simulation and experimental measurement), considering the impact of compressibility and unsteady flow, applying more accurate models like RSM or LES.

Bibliography

[1] N. Adams, *Fluidmechanik, einfürung in die dynamik der fluide, Lecture notes.* Technische Universität München, 2008.

[2] J. Bredberg, *Report on two-equation eddy-viscosity models, Internal report, department of thermo and fluid dynamics chalmers university of technology, göteborg sweden.* 2001.

[3] T. Cebeci and J. Cousteix, *Modeling and computation of boundary layer flows,* Springer, 1999.

[4] R. Geist, "Dampfturbine mit einem drehschieber", ABB Patent GmbH, European Patent Office, EP 0 568 909 A1, 1993.

[5] R. Geist and S. Jürke, "Drehschieber mit mindestens einem axialnadeldrehkranz als drehbewegliches lagerelement", ABB Patent GmbH, Deutsches Patentamt, DE 44 25 344 A1, 1994.

[6] C. Hirsch, *Numerical computation of internal and external flows, Volume 1, the fundamentals of computational fluid dynamics, second edition.* Butterworth-Heinemann, ELSEVIER, 2007.

[7] R. W. Johnson, *The handbook of fluid dynamics.* SPRINGER.

[8] W. Jones and B. Launder, *The prediction of laminarization with a two-equation model turbulence. International journal of heat and mass transfer,15:301-314*, 1999.

[9] M. R. Kariman, "Fluid dynamic investigation of an alternative extraction steam turbine control method: Rotary valve", Dissertation, 2013.

[10] P. Lampart and R. Puzyrewski, "On the importance of adaptive control in extraction/condensing turbines", ASME Turbo Expo, GT2006-91160, 2006.

[11] M. Leschziner, *Statistical turbulence modelling for fluid dynamics-demystified, An introductory text for graduate engineering students.* Imperial College Press, 2015.

[12] F. Menter *et al.*, *The sst turbulence model with improved wall treatment for heat transfer predictions in gas turbines, Proceedings of the international gas turbine congress*, Nov. 2003.

[13] R. Platz, "Industrial steam turbine control", Application Note 83403 (Revision B), USA, 2009.

[14] R.E.Graves and B. Argrow, *Bulk viscosity:past to present, Journal of thermophysics and heat transfer, 13(3):337-342*, 1999.

[15] K. Speicher and E. Mietsch, "Der drehschieber als regelorgan für entnahme- dampfturbinen.", Maschinenbautechnik 15-Heft 4, Berlin. VEB Verlag Technik, 1966.

[16] K. Speicher *et al.*, "Zur entwicklung von niederdruck-dampfsteuerorganen, derzeitiger stand und künftige möglichkeiten", Maschinenbautechnik 38-Heft 1, Berlin. VEB Verlag Technik, 1989.

[17] D. Ting, *Basics of engineering turbulence*. ELSEVIER, 2015.

[18] *User manual of ansys cfx software*.

[19] *User manual of ansys icem software*.

[20] D. C. Wilcox, *Turbulence modeling for cfd, Third ed.dcw industries, la canada, californi*a, 2006.

[21] R. Willinger, *Lecture notes of thermal turbomachines course*. Institute for Energy Systems and Thermodynamics, Technische Universität Wien, Austria, 2015.

[22] R. Willinger, "Beitrag zur aerodynamischen wechselwirkung zwischen axialer turbinenstufe und nachgeschaltetem diffusor", Dissertation, Technische Universität Wien, 1997.

[23] R. Willinger, *Lecture notes of numerical methods for thermal energy systems course*. Institute for Energy Systems and Thermodynamics, Technische Universität Wien, 2010.

[24] R. Willinger, *Numerische strömungsberechnung von thermischen turbomaschinen, Lecture notes*. Technische Universität Wien, 2017.